

# Absorption features of high redshift galactic winds

A. P. M. Fangano<sup>1\*</sup>, A. Ferrara<sup>2</sup> & P. Richter<sup>1,3†</sup>

<sup>1</sup> *Argelander-Institut für Astronomie, Universität Bonn, Auf dem Hügel 71, 53121 Bonn, Germany*

<sup>2</sup> *SISSA/International School for Advanced Studies, Via Beirut 4, 34014 Trieste, Italy*

<sup>3</sup> *Institut für Physik, Universität Potsdam, Am Neuen Palais 10, 14469 Potsdam, Germany*

20 August 2019

## ABSTRACT

The environment of high-redshift galaxies is characterized by both wind-driven outflowing gas and gravitationally infalling streams. To investigate such galaxy-IGM interplay we have generated synthetic optical absorption line spectra piercing the volume surrounding a starbursting analog of a Lyman Break Galaxy selected in a  $z \approx 3$  output from a SPH simulation, including a detailed treatment of mechanical feedback from winds. Distributions for several observable species (H I, C III, C IV, Si II, Si III, Si IV, O VI, O VII, and O VIII) have been derived by post-processing the simulation outputs. The hot wind material is characterized by the presence of high-ionization species such as O VI, O VII, and O VIII (the latter two observable only in X-ray bands); the colder ( $T < 10^{5.5}$  K) infalling streams can be instead identified by the combined presence of Si II, Si III, and C III optical absorption together with O VI that surrounds the cooler gas clumps. However, both line profile and Pixel Optical Depth analysis of the synthetic spectra show that the intergalactic filament in which the wind-blowing galaxy is embedded produces absorption signatures that closely mimic those of the wind environment. We conclude that it may be difficult to clearly identify wind-blowing galaxies and their complex gaseous environment at high redshift in optical QSO absorption-line spectra based solely on the observed ion absorption patterns.

**Key words:** cosmology: theory — galaxies: formation — intergalactic medium — large-scale structure of universe

## 1 INTRODUCTION

Shortly after the first detection of quasi-stellar objects (quasars or QSOs), the presence of many narrow absorption lines in the spectra of these objects was recognized for the first time (e.g., Bahcall (1966)). It soon became clear that these lines (“Ly $\alpha$  forest”) are produced by absorption of neutral hydrogen in gaseous structures that fill the intergalactic space (the InterGalactic Medium, IGM). Today it is widely accepted that the neutral hydrogen Ly $\alpha$  forest traces baryon density fluctuations associated with gravitational instability as part of the large-scale structure formation in the Universe.

With the advent of more advanced spectrographs and larger telescopes, higher quality spectra were obtained and with great surprise it was discovered that the hy-

drogen forest is complemented by absorption lines from heavy elements (Cowie et al. 1995). Subsequent analysis (Ellison et al. (1999), Schaye et al. (2000), Songaila (2001), Simcoe (2006)) have shown that the IGM is enriched with metals at virtually any overdensity and redshift probed, as shown by the observation of resonance transitions associated to ions like C III, C IV, Si II, Si III, Si IV, O VI, and others; the enrichment of underdense regions is still matter of debate (Aracil et al. 2004). A major problem in our current understanding of the IGM is to determine when and by what transport means metals have been able to travel to large distances from their productions sites (presumably, stars in galaxies. It is then clear that the answers to these questions have to come from the study of the physical galaxy-IGM interplay.

One possible mechanism is dynamical stripping. During a close encounter of two or more galaxies, tidal forces can strip away from them part of the enriched gas, which is then dispersed into the IGM. This scenario is particularly important at high redshift, when the encounter rate is enhanced. However, this mechanism turns out to be too inefficient in reproducing the observed metal distribution with H I col-

\* E-mail: fangano@astro.uni-bonn.de

† DFG Emmy-Noether Fellow

‡ Founded by merging of the Institut für Astrophysik und Extraterrestrische Forschung, the Sternwarte and the Radioastronomisches Institut der Universität Bonn.

umn densities (Aguirre et al. 2001). A second mechanism is based on the idea that the energy/momentum deposited by multiple supernovae can drive an outflow of material from the host galaxy (Dekel & Silk (1986); Mac Low & Ferrara (1999), Ferrara & Tolstoy (2000); Madau, Ferrara & Rees (2001); Ferrara, Scannapieco & Bergeron (2005); Springel & Hernquist (2003); Aguirre et al. (2005); Davé & Oppenheimer (2006)). In this scenario, multiple supernova-driven bubbles merge together to form a "superbubble"; the entrapped material would blow-out from the galaxy and vent the hot interior (largely enriched by freshly produced heavy elements) into the IGM giving rise to a large-scale outflow. Yet, the epoch when most of enrichment took place is still unclear. Studies carried out by Songaila (2001), Schaye et al. (2003), Songaila (2005), Ryan-Weber, Pettini & Madau (2006) have shown that the observed CIV absorption characteristics do not evolve significantly in the redshift range  $2 < z < 6$ . This is surprising in view of the fact that most of the star-formation activity in the universe took place at  $z < 5$  (see Hopkins (2004) for an updated compilation). The findings were interpreted as the results of an early ( $z > 6$ ) metal pollution (often referred to as *pre-enrichment*) by the first generation (Pop III) of stars and galaxies (Madau, Ferrara & Rees (2001), Scannapieco et al. (2002)).

With the combined analysis of QSO and galaxy spectra it is possible to connect the properties of the intergalactic absorption lines with that of the foreground galaxies. Using this technique Adelberger et al. (2003) and Adelberger et al. (2005) demonstrated that almost all galaxies at  $z > 2$  can be associated with metal absorbers, in agreement with the earlier theoretical study by Haehnelt, Steinmetz & Rauch (1996), and subsequent analysis by Desjacques et al. (2004), Maselli et al. (2004), Bertone & White (2005), and Kawata & Rauch (2007). While this points directly to the hypothesis that those galaxies are experiencing large scale outflows and hence polluting the IGM *in situ*, the actual mass loss rate and, most importantly, whether they are able to escape the gravitational pull of the galaxy are very hard to assess. Simcoe et al. (2006) have recently analyzed a line-of-sight toward a quasar at  $z \simeq 2.7$  and searched for a correlation between absorbers and nearby galaxies. By constructing detailed ionization models for the different absorbers, they find that their observations indicate a metal-enriched volume of  $\sim 100 - 200 h_{71}^{-1}$  physical kpc around the analyzed galaxies. Furthermore, the sheet-like geometry of the absorbing clouds ( $\Delta L < 1$  kpc) as well as their high metallicity ( $Z > 0.1 - 0.3 Z_{\odot}$ ) suggest an outflow scenario for their origin. Concentrating on low redshifts, ( $z \simeq 0.5$ ) Bouché et al. (2006), starting from a sample of 1806 MgII absorbers, show that their equivalent widths ( $W > 2 \text{ \AA}$ ) are anticorrelated with the absorber halo-mass. Since this indicates that absorbing clouds are not in virial equilibrium with the host-galaxy, they concluded that these absorbers are most probably generated by a starburst activity and expelled via supernova-driven winds. Note that an early-epoch enrichment model is not excluded by this scenario since metals ejected by the first galaxies ( $z \simeq 6-12$ ) should also end up in overdense regions at lower redshifts (Porciani & Madau (2005), Scannapieco (2005)).

The complexity of absorbing cloud populations asks for a careful analysis and interpretation of observational data.

For this aim, simulations can be quite helpful, especially in trying to identify the various gas components that contribute to the gas flow in the intergalactic environment of galaxies. However, simulations are not yet able to follow in detail the full range of physical phenomena that characterize star formation and feedback. So far, the coupling of a consistent modelling of the ISM with a reliable prediction of the physical properties of galactic winds turns out to be quite difficult. New generation numerical codes include often an explicit recipe for starting galactic winds in suitable situations. In these cases of *defaillance*, simulations have to rely on phenomenological prescriptions deduced from theoretical models or inferred from the analysis of the local Universe. To date, the number of observed galaxies with on-going outflows is quite consistent with the theoretical predictions, but the correlation between the outflow and galaxy properties is difficult to be interpreted and shows no substantial trends (Martin (1999), Heckman et al. (2000)). Recently, observations made by Martin (2005) and Murray, Quatert & Thompson (2005) showed a good agreement with theoretical models for momentum-driven winds. In this model, radiation impinges on dust grains, transferring this way its momentum. The latter is moving out of the galaxies and then may couple with the surrounding gas and start an outflow (Murray, Quatert & Thompson 2005). Based on this model, Oppenheimer & Davé (2006) have run a set of numerical simulations using the code GADGET2 (Springel 2005) with a span of feedback prescriptions for galactic winds. They demonstrated that momentum-driven outflows, calibrated via the local universe observations, are able to reproduce a wide variety of CIV absorbers statistics as observed in QSOs spectra.

In this framework of these recent studies we have performed our study. We have used an output from a GADGET2 cosmological simulation that uses state-of-art treatment of multiphase ISM and winds, and keeps track of the contribution of Pop III stars to the overall metal budget. These simulations have been then analyzed with the intention of providing quantitative and clear-cut diagnostics for observational investigation of outflow phenomena around high redshift galaxies; to this aim, and also to clarify the association between absorbing lines and galactic environments, we have performed a spectroscopic analysis around a prototypical galaxy characterized by ongoing wind-activity.

This paper is organized as follows: in §2, we briefly describe the numerical simulation; we then move to the galaxy selection criteria and to the analysis of its gaseous environments. In §3 we analyze the metal absorption features of the "wind region" observed in our spectra and we discuss briefly of the Ly $\alpha$  forest around our target galaxy. In Section §4 we give then our conclusions. In addition, we provide in Appendix A details about the method used to generate our spectra and a summary about the considered metal transitions. Finally, in Appendix B we show our synthesized spectra.

## 2 NUMERICAL SIMULATIONS

Our analysis is based on a hydrodynamic cosmological simulation. The simulation adopts a  $\Lambda$ CDM cosmological model with  $\Omega_M=0.3$ ,  $\Omega_{\Lambda}=0.7$ ,  $\Omega_b=0.04$ ,  $h = 0.7$ , and  $\sigma_8 = 0.8$ ;

periodic boundary conditions are adopted. The numerical code used for the simulation is a modified version of GADGET (Springel, Yoshida & White 2001) modified according to Marri & White (2003), where the interested reader can find the details of the new algorithms introduced. In brief, additions concern: (i) an improved treatment of the multiphase nature of the gas, and (ii) a more refined recipe for stellar feedback. The ISM is modeled as a two-phase medium, made of a cold, dense component and a warm, diffuse one. Once star formation occurs, the feedback energy is distributed to the surrounding particles with a fraction  $e_c$  ( $e_w$ ) incorporated in the cold (warm) phase. Values for  $e_c$  and  $e_w$  could be fixed from a complete theory of interstellar medium, or by specific numerical simulations; in our case these constants were both fixed to 0.4. The remaining 20% of the energy is assumed to be radiated away.

The scheme also tracks the gas metal enrichment due to supernova (SN) explosions by considering a heavy element yield  $y_Z$  such that:

$$\delta M_Z = y_Z \delta M_* \quad (1)$$

where  $\delta M_Z$  is the total metal mass produced per stellar mass ( $\delta M_*$ ) formed. Once metals are produced, a fixed fraction  $f_Z=0.3$  is distributed among the same hot neighbors which receive the feedback energy. Tracking the metallicity allows us to apply the so-called ‘critical metallicity’ criterion introduced by Schneider et al. (2002). According to this criterion, the Initial Mass Function (IMF) of star forming sites is biased towards very massive (PopIII) stars if the metallicity is below  $Z_{cr} = 10^{-4} Z_\odot$ ; above this threshold a switch to a standard stellar population (PopII) with a Salpeter IMF occurs. These stellar populations have distinct feedback prescriptions, depending on the explosion energies,  $e_{sn}$ , and metal production efficiencies,  $y_Z$  of PopIII and PopII stars. Therefore, we adopt the following set of parameters:

$$e_{sn}^{III} = 2.3 \times 10^{50} \text{ erg } M_\odot^{-1} \quad y_Z^{III} = 0.637 \quad (2)$$

for PopIII stars, and

$$e_{sn}^{II} = 4.0 \times 10^{48} \text{ erg } M_\odot^{-1} \quad y_Z^{II} = 0.004 \quad (3)$$

for PopII stars. These above parameters are not yet fully fixed by theory, as the outcome of stellar explosions depend e.g. on progenitor composition, nuclear reactions rates, explosion energy.

We have run simulations at two different resolutions. The low resolution simulation, used mostly as a control run, consists of  $64^3$  particles simulating a  $7.0 h^{-1}$  comoving Mpc; the high resolution run is made up of  $128^3$  particles in a  $10.5 h^{-1}$  comoving Mpc. Both runs have a mass resolution of  $M \approx 10^6 M_\odot h^{-1}$ . In both runs the evolution was followed including the effect of a UV-background (produced by QSOs and galaxies and subsequently filtered through the IGM) whose shape and amplitude were taken from Haardt & Madau (1996). Unless otherwise specified we report results based on the high resolution run.

## 2.1 Target galaxy

As general test for our metal feedback recipe, we have analyzed the low resolution run for the average metallicity of the IGM as traced by carbon, oxygen and silicon. In Fig. 1 we show the relation of these abundances, relative to solar, as a

| Element | Tracer | Abundances |   |
|---------|--------|------------|---|
| [C/H]   | CIV    | -2.58      | -2.82 <sup>1</sup> , -3.47 <sup>2</sup>         |
| [O/H]   | OVI    | -2.14      | -2.82 <sup>1</sup> , [-2.22, -1.3] <sup>3</sup> |
| [Si/H]  | SiIV   | -1.99      | -2.00 <sup>4</sup>                              |

<sup>1</sup> Schaye et al. (2003), <sup>2</sup> Simcoe et al. (2004)

<sup>3</sup> Telfer et al. (2002), <sup>4</sup> Aguirre et al. (2004)

**Table 1.** Abundances values relative to solar from our low resolution run: shown are the considered element (first column), transition used as tracer (second), median value retrieved from our simulation (third), observed values (forth). For a meaningful comparison with observations, we have included in our analysis only pixels with Ly $\alpha$  and metal optical depth higher than  $10^{-3}$ .

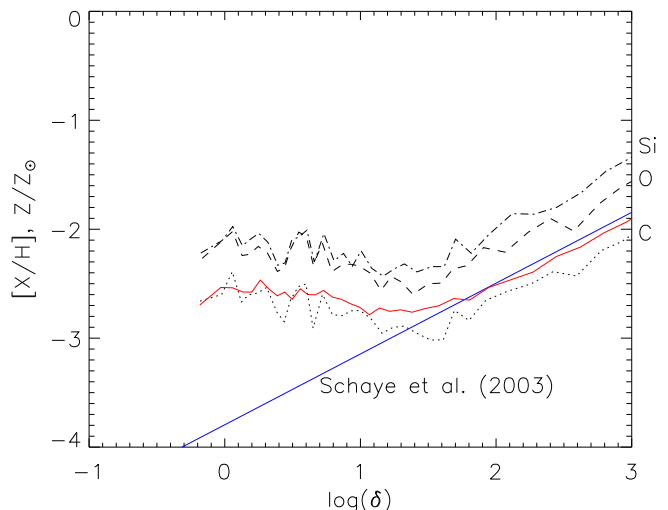


**Figure 1.** Abundances relative to solar for C (dotted), O (dashed) and Si (dot-dashed) as a function of overdensity. The thick red curve represents the values for the total metallicity relative to solar while the straight blue line show the relation found by Schaye et al. (2003) for [C/H] (eq.4).

function of the overdensity ( $\delta \equiv \rho / \langle \rho \rangle$ ). In order to compare with observations, we have limited our analysis to those pixels characterized by optical depths for both Ly $\alpha$  and metal transition  $> 10^{-3}$ . From the plot we deduce that from our simulation a small raise in the metal abundances should be expected at low overdensities where wind effects are more evident. The combined action of our thermal and chemical feedback seems to suggest also the fact that the [C/H] ratio could be the closest numerically tracer of the total metal content of the gas. In the Figure we also show the relation found by Schaye et al. (2003) for [C/H] vs. overdensity:

$$[C/H] = -3.47_{-0.06}^{+0.07} + 0.65_{-0.14}^{+0.10} \times (\log \delta - 0.5). \quad (4)$$

Tab. 1 compares the simulated mean abundances of the three elements/tracers with the observational values. From the joint analysis of Fig. 1 and Tab. 1 we conclude that our model is quite successful in reproducing both Schaye relation and the level of pollution in the IGM as derived by

QSOs absorption lines. This strengthens our confidence on the implemented feedback scheme.

In order to quantify and diagnose the effects of feedback and winds on galactic environments, the first step is to identify a suitable representative target galaxy in the simulation box showing a strong wind. To this aim, we have searched in the high-resolution run output at  $z = 3.26$  for high density ( $n > 10^{-2} \text{ cm}^{-3}$ ), high temperature ( $T > 10^6 \text{ K}$ ) particles. The latter condition ensures that we are dealing with a galaxy that is surrounded by shocked gas; however, such high temperatures can also be reached during virialization and/or infall, so they do not necessarily imply that the object is experiencing a wind phase. We thus complement the high-temperature condition with that of a high peculiar particle velocity, as infalling material is likely slowed down by the interaction with the halo gas. The total mass of the selected target galaxy which fulfills the above listed conditions is  $\approx 10^{11} M_{\odot}$ , i.e. a mass typical for Lyman Break Galaxies (LBG). In the chosen volume, the average metallicity is  $\approx 10^{-2} Z_{\odot}$ .

## 2.2 The target galaxy environment

In Fig. 2 we show 2D maps of different quantities (temperature and velocity field, ram-pressure, total metallicity, Pop III stars contribution to the latter) in a plane across the target galaxy center. The signature of the wind is clearly seen as a region of enhanced temperature in the corresponding map, with a typical (physical) size  $\simeq 0.4 \text{ Mpc}$ . The shock caused by the outflow has heated up the gas to a temperature  $\simeq 10^6 \text{ K}$ , but the outflowing gas is being slowed down by the infalling material. We refer to this region as the (wind) *bubble*.

The interplay between the infalling and outflowing material shapes the bubble geometry, producing significant deviations from the commonly assumed spherical symmetry. Instead, we find that the shape of the bubble is better described by a pancake-like geometry with a radius-to-thickness ratio of  $\simeq 2 : 1$ . The bubble extends almost orthogonally to the *filament* that hosts the galaxy, with 4 or more lobes caused by the infalling material, which we denote as (infalling) *streams*. An interface between the wind bubble and a stream is clearly identified by the low pressure arc (right top panel) to the left of the bubble; there, the outflowing material is actually stopped by the ram-pressure of the infalling gas causing the formation of a thin, dense shell. The analogous shell formed at the top lobe is barely recognizable as it has already started to recollapse onto the galaxy. To the right hand side of the bubble instead the collapse evolution is more advanced and the infalling material is almost freely penetrating into the hot bubble. As a result, the velocity field is very complex with regions of outflowing and infalling motions with peculiar velocities up to  $250 \text{ km s}^{-1}$ . Inside the galactic environment, the infalling material is re-directed by the galactic activity and trapped within the hot bubble. From the maps shown here we cannot identify any outflow channel through which the gas could escape the bubble. Inside the bubble, the material now is heated to temperatures  $T \gtrsim 10^6 \text{ K}$ .

The spatial distribution of the metallicity (lower panels) is very similar to the temperature, clearly indicating that the bubble has been created by supernova explosions within the

target galaxy. However, the metallicity pattern corresponding purely to PopIII stars requires a previous star formation activity which pollutes the streams. This is deduced from PopIII-enriched cold clumps falling toward the galaxy seen in the upper portion of the map. Such clumps have been produced at earlier cosmic times by progenitors of the target galaxy and later became part of the accretion process feeding it. They are pushed and compressed by the pristine material lying behind them and streaming from the filament into the bubble (see temperature map). These kind of condensed clumps in the bubble had enough time to cool down to temperature  $T < T_W \equiv 10^{5.5} \text{ K}$ ; throughout the following we identify these structures as *cold clumps*. Note that also the filament contains metals, the chemical composition being dominated by the first generation of stars. We find that PopIII contribution to the total metal content of the filament is  $> 30\%$ . Metal absorption arising in filamentary gas therefore is important to study the nucleosynthesis of the first objects.

In summary, the galaxy environment is characterized by two different environments: (i) the filament in which the galaxy is embedded, and (ii) the wind environment, in turn constituted by the wind bubble, infalling streams and cold clumps accreting onto the galaxy.

## 3 IONIZATION ANALYSIS

Having selected the target galaxy and characterized its environment, we now investigate their properties by means of synthetic absorption spectra that can be directly compared with observed QSO absorption-line data. To this aim, we have analyzed  $\sim 1600$  lines of sight (LOS) through the selected volume<sup>1</sup>. The ionization equilibrium, under the influence of the UV background adopted in the simulation, has been calculated in each of the ( $\sim 100$ ) cells into which each LOS has been segmented, using the code CLOUDY96<sup>2</sup> (Ferland et al. 1998). For the following analysis we have used either the Pixel Optical Depth (POD) technique described in Cowie & Songaila (1998) and Aguirre et al. (2002), or the automated Voigt-profile fitting using the code AUTOVP (Davé et al. 1997), depending on the specific question addressed. For further details on the simulated spectra we refer to Appendix A.

As a first step to search for possible tracers of circumgalactic high-temperature regions, we have analyzed the gas temperature distribution shown in Fig. 3 (upper panel). The horizontal width of these lines denotes the temperature range in which the transmitted flux,  $F = e^{-\langle\tau\rangle}$ , due to a given ion opacity is  $F < 0.95$ , a level denoted also by the dashed line in the lower panel. The vertical position of the lines indicates the fraction of cosmic baryons polluted with that ion (we have defined a pollution threshold by requiring a ionization fraction  $> 10^{-2.5}$  for each species) integrated over the above temperature range. The distribution shows a peak at  $T \approx 2 \times 10^4 \text{ K}$ , accounting for about 20% of the baryonic fraction in the volume; an almost equal amount of matter resides at  $T \gtrsim 10^5 \text{ K}$ . CIV traces almost the same

<sup>1</sup> The selected region size is of  $1.2 \times 0.5 \times 0.5$  physical Mpc.

<sup>2</sup> <http://www.nublado.org>

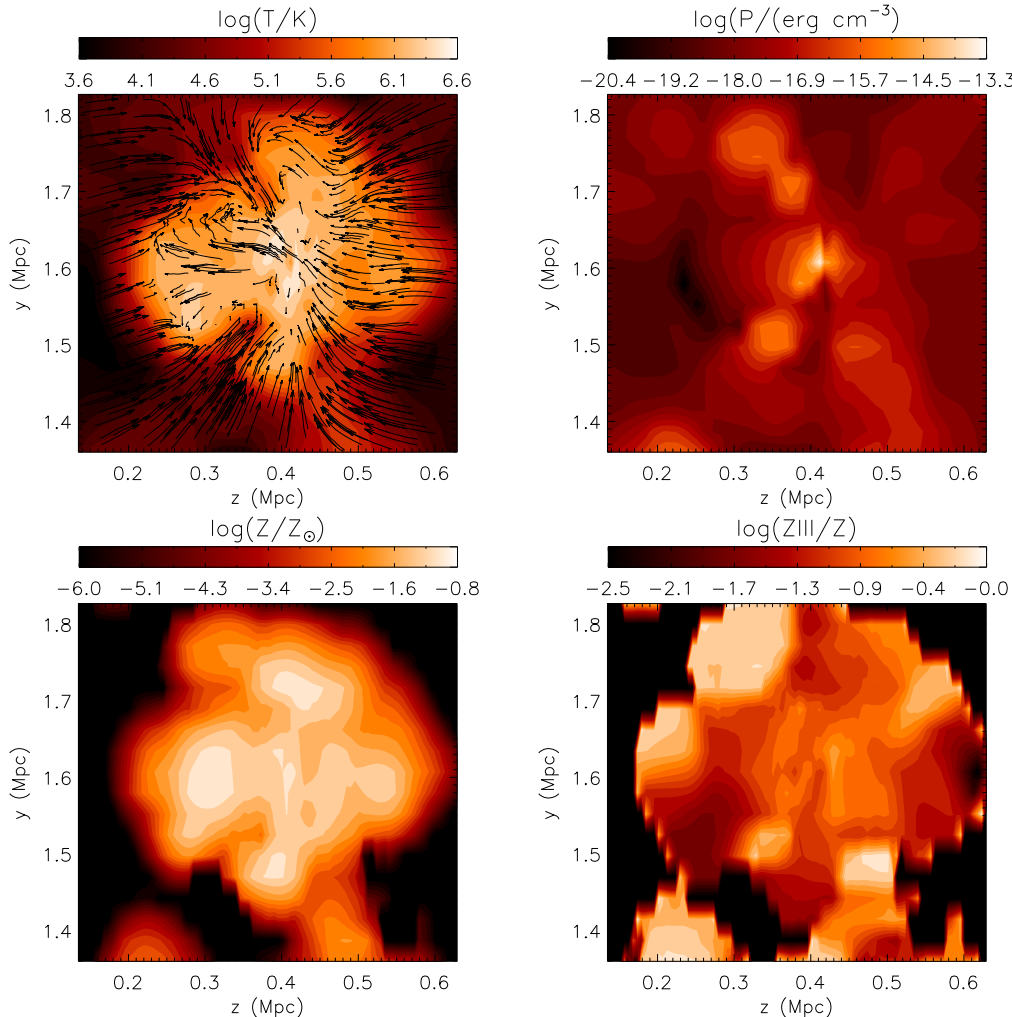


**Figure 2.** Maps of various quantities across the target galaxy center. *Upper left:* temperature and peculiar velocity field (arrows; the largest one corresponds to  $250 \text{ km s}^{-1}$ ); *Upper right:* ram-pressure; *Bottom left:* total metallicity; *Bottom right:* PopIII-to-total metallicity ratio. Sizes are in physical units.

amount (about 0.6%) of baryons as  $\text{SiIV}$ , but it is sensitive to a slightly higher temperature regime. A similar trend is found for oxygen ions with  $\text{OVI}$  spanning a relatively narrow range around the peak temperature ( $\approx 3 \times 10^5 \text{ K}$ ) for collisional ionization of  $\text{OVI}$ , whereas  $\text{OVII}$  extends for almost 1.5 dex. We find that 0.1-0.2% of all the baryons should be already contaminated with these species at  $z \approx 3.26$ .

The mean transmitted flux for these ions varies as a function of temperature. These profiles are useful to understand the physical origin of a given ion. The double peak feature seen for  $\text{CIV}$ ,  $\text{SiIV}$  and  $\text{OVII}$ , shows the distinct effect of the radiative and collisional ionization processes, with the high temperature peak being associated with collisionally ionization and the other one (typically less pronounced) resulting from photoionization. Therefore, for any given species, the relative strength of these two features gives a measure of the importance of photo- and collisional ionization. In particular,  $\text{CIV}$  has a higher contribution from collisional ionization than  $\text{SiIV}$ . An important point is that both  $\text{OVI}$  and, even more evidently,  $\text{OVII}$  are produced by collisional ionization, and therefore they represent particu-

larly useful diagnostics to study the hot intergalactic environments like wind cavities.

In the following we characterize in detail the absorption patterns associated with the two types of target galaxy environments introduced above, i.e. the wind and the filament environment.

### 3.1 Wind environment tracers

As already pointed out, inside the volume enclosed by the supernova-driven shock three different gas phases/structures coexist: infalling streams, cold clumps and hot, outflowing gas. As seen from Fig. 4, in which we show the spatial distribution of the ionization fractions of various ions, the bubble interior is characterized by a very low  $\text{HI}$  abundance ( $\log f_{\text{HI}} < -6$ ), caused by the enhanced collisional ionization rate associated with the high gas temperature. Such low abundance in the central regions is common to most of the species shown, with the only significant exception of  $\text{OVI}$ . The latter species appears to be almost homogeneously distributed in the volume, although its abundance

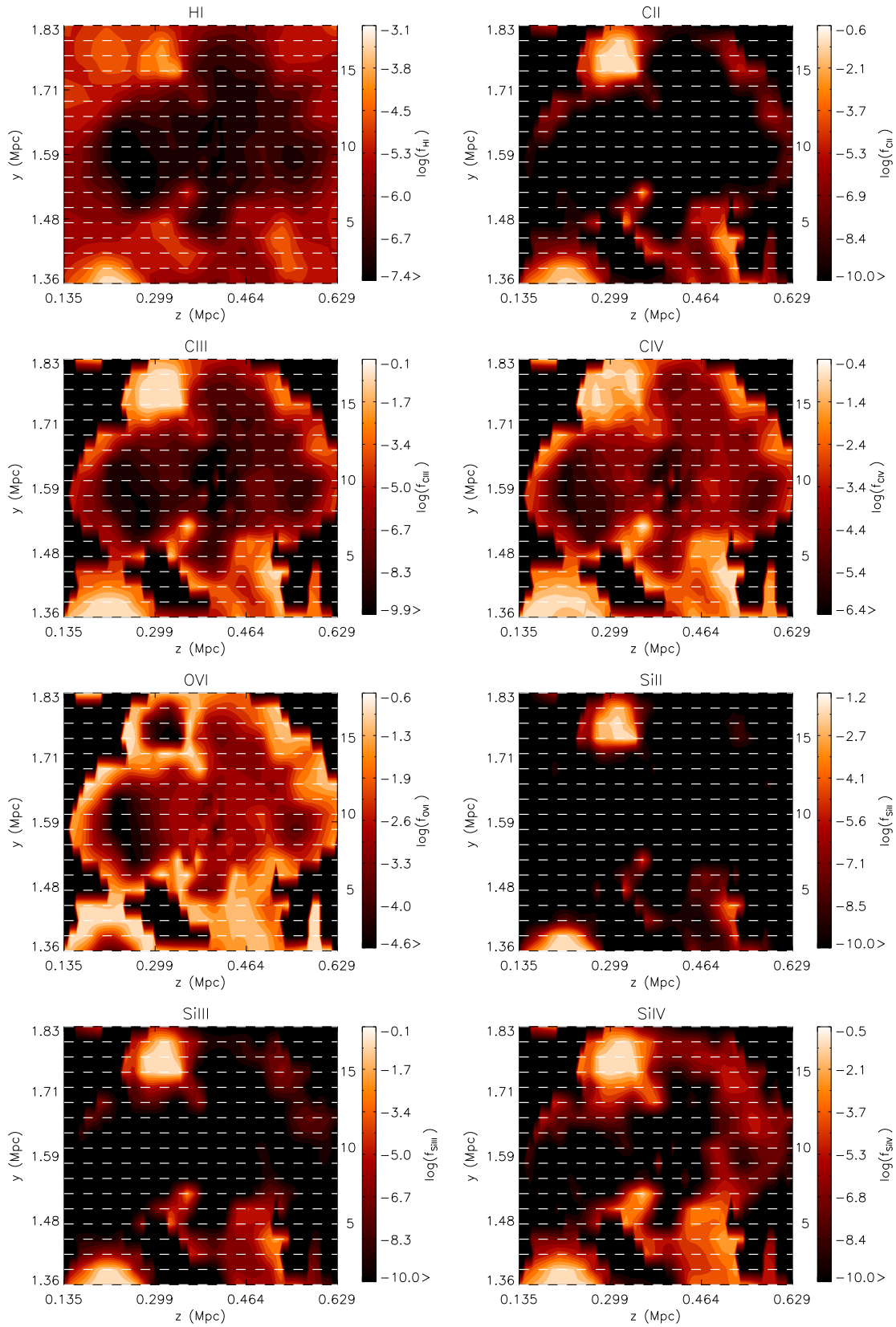


**Figure 4.** Ionization fractions (i.e, the fraction of the  $X$  element in the ionization state  $i$  with respect to its total abundance,  $f_{X,i} = n_{X,i}/n_X$ ) maps across the target galaxy center for various ions are shown. The dotted lines indicate the analyzed line of sight (LOS), numbered from 1 to 18 as labeled to the right of each panel.

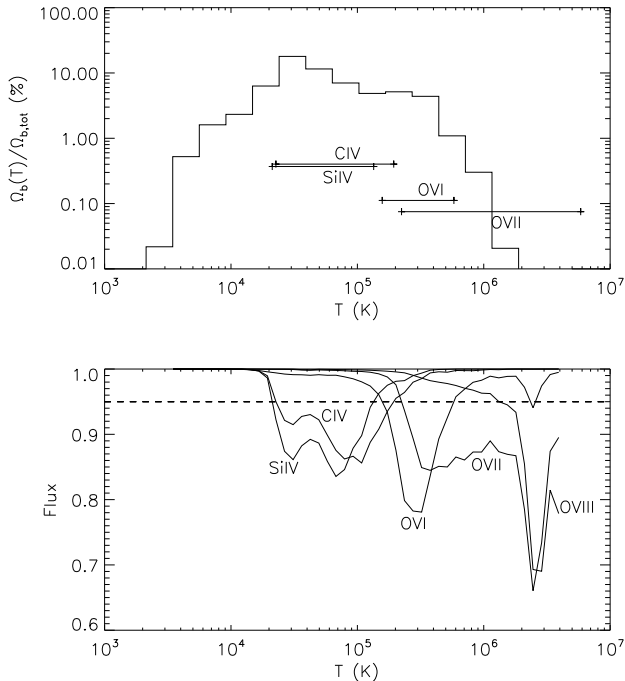


**Figure 3.** *Upper panel:* temperature distribution of the baryonic fraction. Horizontal lines mark the temperature range in which the indicated ion produces a mean transmission of  $\simeq 0.95$ ; their vertical positions refer to the fraction of cosmic baryons polluted with that ion. *Lower panel:* mean transmitted flux,  $F = e^{-\tau}$ , for the different ionic species as a function of gas temperature.

drops in isolated regions: the most noticeable example are the OVI “voids” seen on the upper-left part of the distribution map for this ion. Guided by the previous discussion on the nature of the different structures in the target galaxy environment, we interpret such OVI voids as cold clumps that condensed out of the expelled material and now falling back towards the galaxy. In addition to OVI (which appears to be the best wind tracer) the bubble region is characterized by considerable abundances of OVII and OVIII (for a detailed view see Appendix C, Fig. B6 and Fig. B7). Although currently unavailable in high-redshift observations these ions would represent very reliable tracers of active outflow regions.

In addition to hot gas (which has a very complex/turbulent velocity field, resulting in either outflowing or infalling flows) we have noticed the presence of cooler gas, either in form of infalling streams or isolated clumps. These cool phases are best traced by low-ionization species such as CII, CIII, SiII, and SiIII. For example, these ions have enhanced abundances in the cold gas clump previously identified in the upper left region of the maps. Intermediate ionization ions (CIV and SiIV) are instead typically found in the interfaces between the cool and the hot gas phase. It is worth noticing that while SiIV has a more patchy distribution concentrated around the clumps, CIV extends deeper into the bubble region and thus into higher temperature regions, as noticed previously (Fig. 5, left panel). A first qualitative conclusion drawn from the maps is that the bubbles could be identified by searching for absorbers that simulta-

neously have low SiIV/CIV ( $\log(f_{\text{SiIV}}/f_{\text{CIV}}) < -2$ ) and very high OVI/CIV ( $\log(f_{\text{OVI}}/f_{\text{CIV}}) > 1$ ) ratios. These conclusions are visually supported by the two maps showing the spatial distribution of these ratios reported in Fig. 5; typical examples for this behavior are seen in the spectra obtained from LOS #10 and #14 shown in Fig. 6, where we present a selection of absorption spectra through the bubble environment along the LOS defined in Fig. 4. Both LOS exhibit strong OVI and weak CIV absorption systems caused by infalling ( $v > 0$ ) material, but no SiIV is detected. Despite the higher CIV ionization fraction along LOS #13 (Fig. 4) no CIV absorption is seen along this sightline (Fig. 6) due to the very low gas densities sampled by that LOS. Stated differently, a non-detection of CIV absorption does not necessarily imply a deficiency of that ion. Instead, its distribution in physical and/or velocity space could be such that the corresponding absorption is smeared out. Only sightlines piercing regions of enhanced density (e.g. LOS #14) and/or located nearby the target galaxy (LOS #10) exhibit clear signs of CIV absorption.

The cold clump itself instead is characterized by the presence of SiII, SiIII and SiIV. It appears that the volume occupied by a given element (here Si) increases with its ionization state; the same conclusion holds for carbon ions CII, CIII and CIV. Typical absorption patterns arising from the clump structures can be seen in LOS #15, #16 and #17 shown in Fig. 6. Absorption features arising from ions with similar ionization states (e.g., SiIII and CIII) are well aligned in radial-velocity space, although some ions may be more spatially extended than others (e.g., CIV vs. SiIV). The contiguity with the hot gas in which the clump is immersed gives rise to a broad interface region and causes a OVI absorption velocity shift of  $\Delta v \simeq 25 \text{ km s}^{-1}$  with respect to SiII (LOS #16). It is worth noticing that along LOS #16, piercing the clump, doubly-ionized species (CIII and SiIII) are heavily saturated (see Fig. 6).

### 3.2 Comparison with the filament environment

As we have discussed, the target galaxy and its wind bubble are embedded in a cosmic filament essentially aligned perpendicular to the plane of the maps shown in Fig. 1, i.e. its symmetry axis is parallel to the  $x$ -direction. In order to investigate the spectral differences between the wind and the filament environments, we have compared LOS passing through the wind bubble and those intersecting the filament (hence at an  $x$  elevation larger than the bubble radius  $\approx 0.2$  physical Mpc).

To anticipate the main point of the following analysis, we find very difficult to discriminate cosmic web structures from those created by the galactic wind purely from available absorption data. The main reason is that cold clumps resulting from the fragmentation of the supernova-driven shell have properties that hardly differ from those of the filament hosting the system.

To further elucidate this point, let us consider a LOS passing through the bubble on the  $y-z$  plane identified by  $x = 0$ ; such line will cross the cool clumps/shell delimiting the hot cavity. Most of the absorption systems will arise from these dense structures rather than from the hot, rarefied interior. Thus, although the latter gas has well defined abundance ratios (e.g. high OVI/CIV, low SiIV/CIV as found

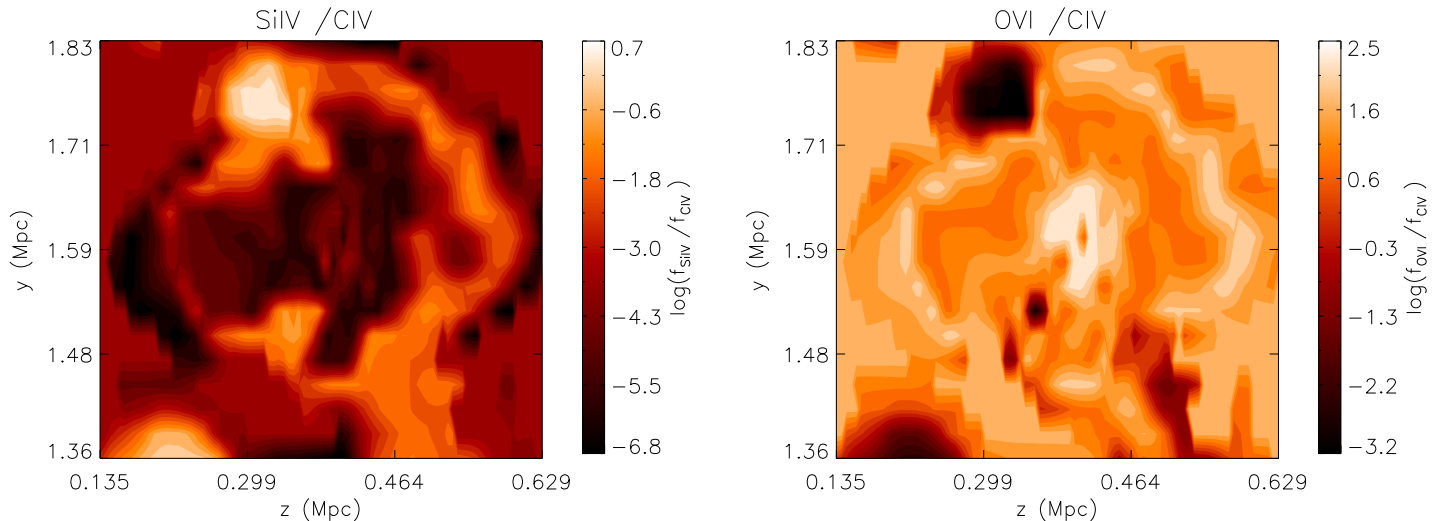


**Figure 5.** Spatial distribution of SiIV/CIV (left panel) and OVI/CIV (right) ratios in the simulated volume around the target galaxy at  $z = 3.26$ . Sizes are in physical units.

in the previous analysis of this phase), their absorption signature is too weak to be detected; on the contrary, the most evident absorption features come from the cool component. These will not be different from those obtained from the analysis of a LOS passing at higher  $x$  through the filament only, given that the physical conditions in the two structures are similar.

It has to be noted that these similar physical conditions originate from different thermal histories. The cool clumps and shell are the product of the radiative cooling of the shocked bubble gas from high temperatures,  $T \approx 10^6$  K. In the simulation accretion shocks are clearly seen in the filaments, too (this fact was first pointed out by Cen et al. (1994)) and these induce complex interface structures which harbor OVI and other highly ionized species. Stated differently, the effect of supernova-induced shock is not easily disentangled from shocks associated with the gravitational collapse of small scale structures giving rise to the overdensities we identify with the Ly $\alpha$  forest<sup>3</sup>.

A more quantitative conclusion on this issue might come from the POD analysis of the synthetic spectra presented in Fig. 7. Shown are the optical depths of various low- and high-ionization species plotted against the H $\alpha$  Ly $\alpha$  optical depth in the filament and in the wind environment. To correct for saturation, we have complemented the Ly $\alpha$  line with the weaker Ly $\beta$  and Ly $\gamma$  transitions. The two vertical dotted lines indicate the saturation point (i.e. when absorption reaches 85% of the continuum level) for Ly $\alpha$  and Ly $\beta$ , respectively, showing from left to right the regions where these three transitions were used. To compare our results with observations, we applied the same analysis to a sample of 28 absorption systems found in 13 spectra from the VLT/UVES Large Program "The cosmic evolution of the IGM" (J. Bergeron et al.) which provides high S/N, high spectral resolution IGM data for  $z \simeq 3$  (see Tables A1, A2).

Despite the fact that we are tracing high density regions, metals are detected down to Ly $\alpha$  optical depth

$\simeq -2.0$ . This is mostly due to the high signal-to-noise ratio [ $S/N(\text{CIV}) \simeq 150$ ,  $S/N(\text{OVI}) \simeq 98$ ] at the redshift considered. Unfortunately, a clear distinction in the behavior of the various ions in the two environments does not emerge: both the filament and the wind LOS opacities share almost the same trend with the Ly $\alpha$  optical depth. As expected, SiII and OVI are complementary tracers for the H $\alpha$  absorption. SiII traces mostly the high-density clouds while OVI is present in lower density regions. In simulated spectra half of the H $\alpha$  absorbers, almost regardless of their physical properties, do not exhibit OVI absorption. The existence of these sub-sample lowers the mean OVI optical depth and causes the second plateau at high Ly $\alpha$  optical depth, where the number of high OVI optical depths points has a drop. There is a good agreement between our simulated data and the observations for almost all ions, with the only exception of SiIV and, to a lesser extent, of OVI. This is most probably due to a selection effect in our sample of absorption systems. For the OVI our sample does not represent properly the OVI-free absorbers at high Ly $\alpha$  opacities. As for SiIV, the shift of +0.75 dex seen between predicted opacities and the data is due to the fact that observed systems are more biased towards intermediate column density absorbers and they are characterized by very shallow lines; while in our spectra almost all the H $\alpha$  absorbers with column density  $\log N_{\text{HI}} \simeq 13.8$  are associated with relatively strong SiIV absorbers.

In addition to the optical depth, the shape and width of the absorption systems provide additional physical information that might be in principle used to distinguish between absorbers in the bubble and in the filament. In fact, these environments are expected to be dynamically very different. In Fig. 8 we show the Doppler parameter distributions for the transitions considered (as obtained from Voigt profile fitting) in the filament and bubble environment. Once again, and for the reasons explained above, no significant differences between the two distributions emerge for the considered ions.

<sup>3</sup> A similar effect has been noted by Kawata & Rauch (2007)



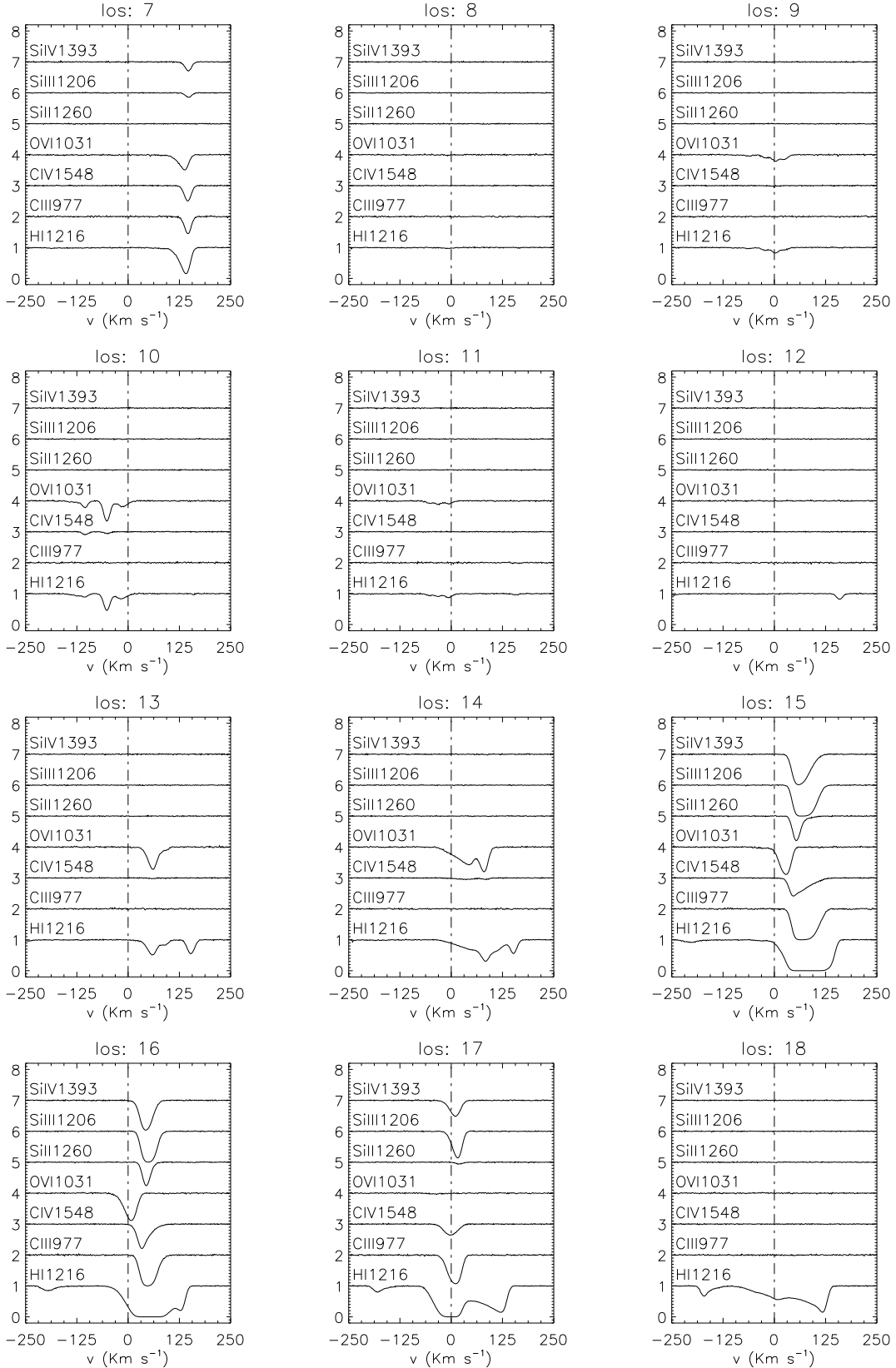


**Figure 6.** Absorption systems for the LOS #7-18 (labeled at the top of each panel) through the wind bubble; see Fig. 4 for their positions and ionization conditions. Negative (positive) velocities denote approaching (receding) flows with respect to the observer.

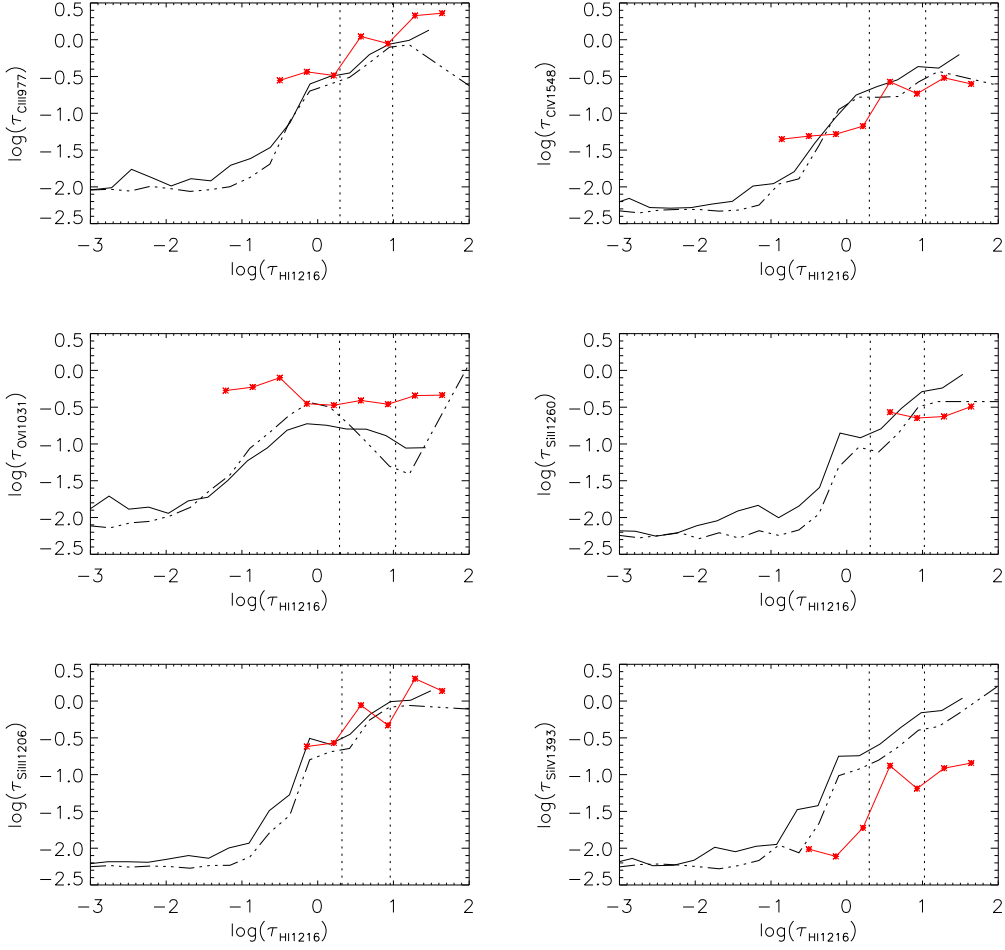


**Figure 7.** Pixel optical depth analysis results for the synthetic spectra. Plotted are the optical depths of various low- and high-ionization species against the HI Ly $\alpha$  optical depth in the filament (solid lines) and in the wind (dashed-dot) environment; the starred line represents observational data from the VLT/UVES LP (see Tab. A1 and Tab. A2). The two vertical lines mark the points at which Ly $\alpha$  (leftmost) or Ly $\beta$  (rightmost) absorption reaches 85% of the continuum level. Only bins with more than 50 data points are shown.

### 3.2.1 Alternative strategies

As pointed out before, the bubble environment is characterized by  $\log T > 5.5$  and highly ionized species such as OVI, OVII and OVIII (Fig. 2, 3). Among these ions, only the OVI transition falls within the UVES wavelength range, while those of OVII ( $\lambda = 21.6 \text{ \AA}$ ) and OVIII ( $18.97 \text{ \AA}$ ) are located in the X-ray band and will be observed by future X-ray facilities. It is interesting to briefly outline the general trends of the optical depth distribution also for these species.

The optical depth for each transition has been computed using the following *in situ* approximation (Theuns et al. 1998):

$$\tau(k) \simeq n_x(i) \Delta_{px} \frac{(\sigma_0 f \lambda_0)}{1+z} \frac{c}{\sqrt{\pi} b_x(i)} \Phi_{Gauss}(k), \quad (5)$$

where the symbols are defined after Eq. A2 and the physical properties of the gas are taken from the output of the numerical simulation. To check the sensitivity of the optical depth to temperature, as a test we have fixed the density to the typical values found in the bubble and in cool/filament re-

gions, that is  $\log \langle n \rangle \approx -3.7$  and  $\log \langle n \rangle \approx -2.7$ , respectively. In Fig. 9 we show the predicted OVII/OVIII optical depths (normalized to the corresponding OVI one) as a function of temperature for both environments. The optical depths for OVII and OVI become equal for temperatures  $\log T \approx 5.6$  in both environments; the ratio between OVIII and OVI optical depths becomes equal to unity at higher temperatures in the bubble region ( $\log T \approx 6.0$ ) than in the filament ( $\log T \approx 5.7$ ). Both OVIII and OVII are then expected to provide larger opacities at high temperatures ( $\log T \geq 5.5$ ) with respect to OVI, implying that these species would be particularly well suited to study the hot component of high redshift galactic winds.

### 3.3 Additional filament properties

Finally, we briefly present a statistical analysis of the HI Ly $\alpha$  forest in the filament region in which the target galaxy and its wind bubble are embedded. As the cosmic volume we are considering is biased by the presence of the relatively massive target galaxy, we do not expect it to be representative of

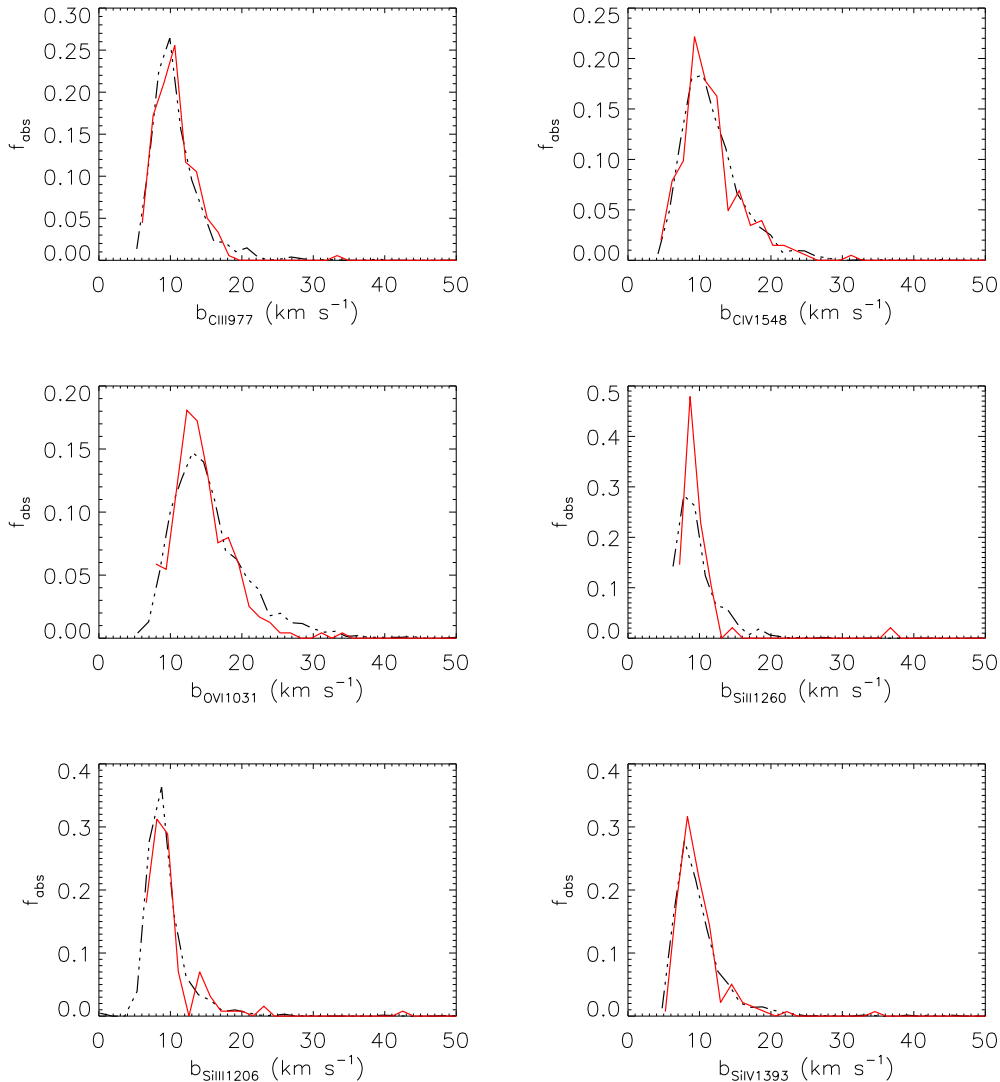


**Figure 8.** Simulated Doppler parameter distribution for the different ions. Dotted (solid) lines refer to the filament (bubble) environment.

the typical low-density environments sampled by Ly $\alpha$  forest observations. Nevertheless, it is intriguing and instructive to evaluate the possible differences.

To compare our sample of H I absorbers with the observed properties of the Ly $\alpha$  forest in high-redshift spectra we have used the data published by Kim et al. (2002). These consist of Ly $\alpha$  absorbers analyzed by Voigt profile fitting of the spectra of 8 QSOs covering the Ly $\alpha$  forest at redshift  $1.5 < z < 3.6$  obtained from VLT/UVES observations. For consistency, we have only used a sub-sample of quasars with  $z > 3$ . The results of this comparison in terms of the neutral hydrogen column density,  $N_{\text{HI}}$ , and Doppler parameter distributions are shown in Figs. 10-11. The agreement in terms of the  $N_{\text{HI}}$  distribution is generally good in the range  $13 < \log N_{\text{HI}} < 15$ . The very low column density deficiency can be possibly caused by the different behavior of the data analysis software used for the two studies. In Kim et al. (2002) the study was carried using VPFIT (Carswell et al.) compared to which AUTOVP seems to un-

derestimate the number of low column density absorbers. Although data incompleteness can also play a role. As for the Doppler parameter, the mean of the simulated sample is shifted towards values that are lower than the observed one. This is plausible if we consider that in our volume we have large amounts of dense and cold gas (i.e. filament gas) causing narrow absorption features due to the reduced thermal line broadening.

## 4 CONCLUSIONS AND DISCUSSION

In this work we have presented an analysis of artificial absorption-line spectra from the circumgalactic and intergalactic gas of a wind-blowing galaxy selected from a  $z \sim 3$  output from a SPH simulation. The simulation includes both a multiphase treatment of the interstellar medium (ISM) and a consistent picture for the chemical enrichment of the Universe (Bruscoli et al. 2003). With our feedback scheme

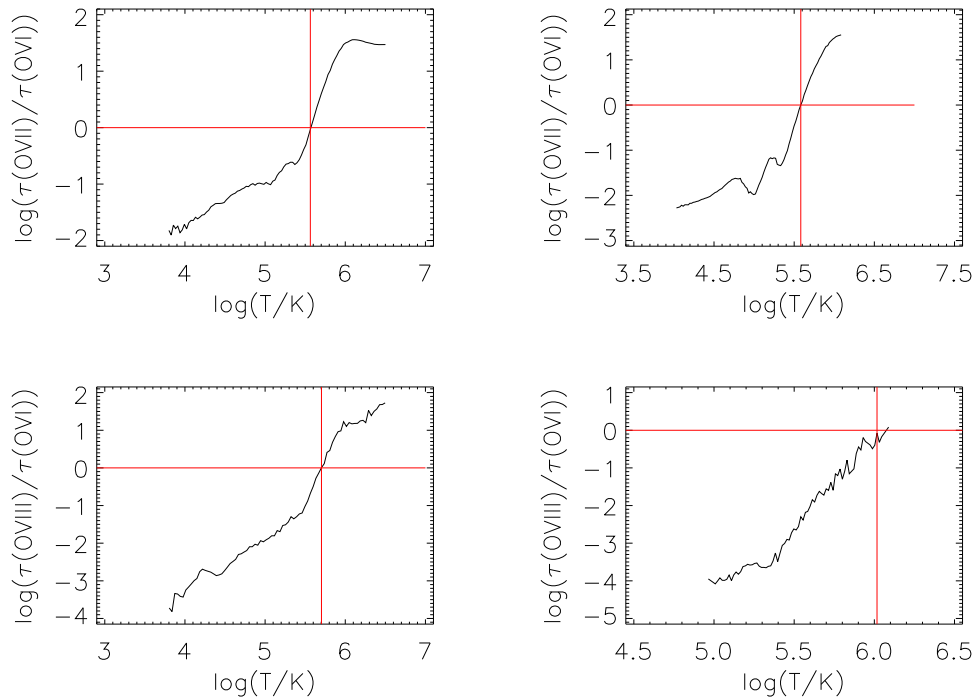


**Figure 9.** Ratios between OVII and OVI (upper row), and OVIII and OVI (lower row) optical depths. The left (right) column refers to the filament (bubble) region. The vertical red lines indicate the temperature where the two optical depth become equal.

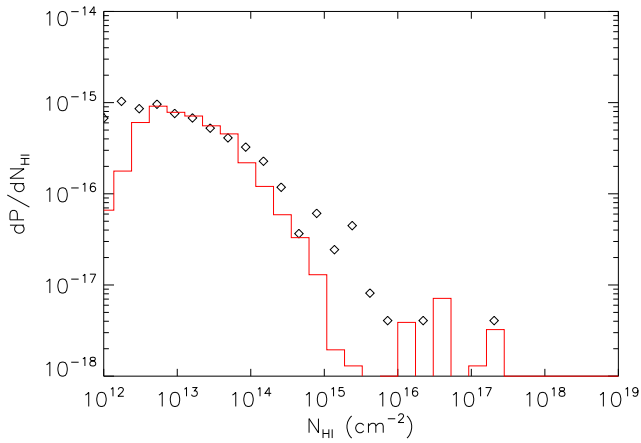


**Figure 10.** Comparison between the HI column density distribution of the absorbers in the simulated galaxy environment (red line) and the observed sample (diamonds). Data are taken from Kim et al. (2002).

we are able to reproduce the observed values for  $[C/H]$ ,  $[O/H]$  and  $[Si/H]$  without requiring an overall constant pollution of the IGM as well as the relation between  $[C/H]$  versus overdensity found by Schaye et al. (2003).

The simulated object is comparable in mass with a LBG at this redshift. The spectra were generated to mimic the behavior of the UVES spectrograph.

For the wind bubble we find that the interplay between the cooler infalling material and the outflowing hot

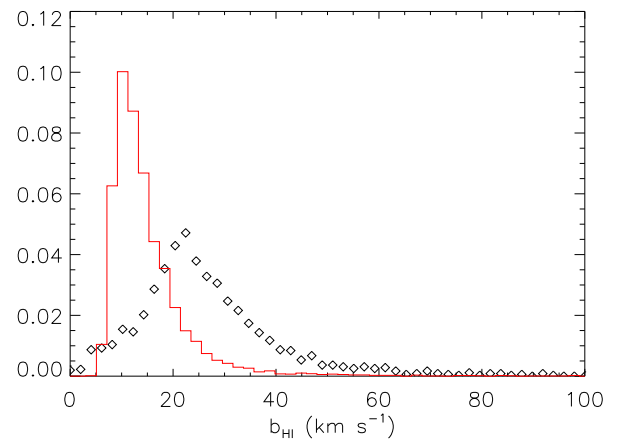


**Figure 11.** Comparison between the HI Doppler parameter distribution of the absorbers in the simulated galaxy environment (red line) and the observed sample (diamonds). The observational data are taken from Kim et al. (2002).

gas shapes a bubble-wind geometry, causing a topology more similar to a pancake like geometry developing orthogonally to the filament hosting the galaxy, leaving the filament almost undisturbed. We identify more than four lobes caused by the cold-bubble material, separated by the so-called infalling-channels. If this is typical for wind-blowing galaxies at high redshift, then the gaseous environment is determined by: (i) the cold filament hosting the galaxy, (ii) a mixture of hot gas ( $T > 10^5$  K) filling up the cavity created

by the galactic wind, (iii) the almost pristine IGM infalling towards the galaxy and opposing to the hot-bubble expansion, (iv) the colder blown out material that could have had the time to fragment into smaller clumps.

From the spectral analysis we find that cold-bubble clumps are characterized by SiII, SiIII, CII and CIII absorption. High oxygen ions lines are not expected in these clumps, but the cooler gas (as indicated by SiII absorption) is enveloped by an OVI phase.

The outflowing gas from the galaxy is characterized by the high ionization states of oxygen, i.e., OVI, OVII, and OVIII. While only OVI is observable in UV/optical absorption, we show that the OVII and the OVIII phase should give rise to absorption with substantial optical depths in the X-ray band.

A physical environment similar to that of the cold clumps within the bubble is present in cooler regions in the surrounding intergalactic filament (i). Here, the cold and warm filamentary material produces low- and high ion absorption patterns that mimic those found in the bubble environment. From an analysis of the optical depth and velocity width distribution of the absorption in both environments we find that there is no clear way to distinguish between these two spatially very distinct environments based on their absorption-line patterns.

The comparison of our optical depths with the observed data shows a good agreement for almost all ions except for OVI and SiIV. This is most likely due to the composition of our observed sample. In our simulated spectra, half of the LOSs showing strong Ly $\alpha$  optical depths do not show appreciable OVI absorption; while our observed sample lacks in these systems causing a higher mean OVI optical depth. As concerning SiIV, our observed sample is mostly composed by intermediate column density absorbers. In our simulated spectra instead, higher H $\alpha$  column densities absorbers are preferably associated with medium/high column densities SiIV absorbers.

Our study suggests that it is quite difficult to discriminate between the various circumgalactic and intergalactic gaseous phases of a starbursting galaxy environment based solely on the absorption line characteristics. Enlarging the sample of target objects would probably increase the statistical weight of our conclusions, but we do expect that the general picture is preserved. The incidence of cold clumps on the spectra is expected to increase in more complex environment, as for example if more filaments are intersecting each other. Along with a different metal distribution, bubbles will be instead characterized by almost the same range of temperatures and densities; they will then give rise to very similar absorption patterns. Metal cooling can then be the most important missing ingredient of the present study. Non-equilibrium ionization effects could also leave an imprint on the cooled gas, which might still keep memory of the past hot and rarefied condition. We are planning to explore these variables on future works.

Finally, a brief comparison with two recently appeared studies (Oppenheimer & Davé (2006); Kawata & Rauch (2007)) must be given.

In Oppenheimer & Davé (2006) the authors mainly use statistics related to CIV absorption to compare their different feedback recipes with observational result. Consistently

with their findings, we confirm that most of the CIV is of collisional origin; however, our results also reproduce the [C/H] vs. overdensity relation by Schaye et al. (2003). Most probably, this discrepancy is due to a different metallicity distribution. Oppenheimer & Davé (2006) predict a metallicity  $\simeq 1$  dex higher than our values; also their fiducial models show an almost flat pollution at high overdensities (see their Fig. 10) contrary to our continuously rising level. Still, both works predict that winds expand preferably in low density regions, leaving the filaments hosting the galaxy unaffected.

As for Kawata & Rauch (2007), their main finding is that OVI is the ion most sensible feedback tracer. Their assumption of a constant - and somewhat unphysical - IGM pollution does not allow a direct comparison with our metallicity distribution. Nevertheless, by looking at their maps it seems that the bulk of the OVI absorption arises from shocked filament material as well as from clumps condensed from blown out gas, a scenario in agreement with the one proposed here. Repeating their search for strong OVI absorbers (with flux  $> 0.8$ ) associated with unsaturated H $\alpha$  ones, we find that these systems are almost evenly produced in the bubble environment and the filament one. We cannot then confirm the exclusive association of these systems to winds.

## REFERENCES

- Adelberger K.L., Steidel C.C., Shapley A.E. and Pettini M.: 2003, ApJ, 584, 45
- Adelberger K.L., Shapley A.E., Steidel C.C., Pettini M., Erb D.K., Reddy N.A.: 2005, ApJ, 629, 636A
- Aguirre A., Hernquist L., Schaye J., Katz N., Weinberg D.H. & Gardner J.: 2001, ApJ, 561, 521
- Aguirre A., Schaye J., & Theuns T.: 2002, ApJ, 576, 1
- Aguirre A., Schaye J., Kim T., Theuns T., Rauch M., Sargent W.L.W.: 2004ApJ, 602, 38A
- Aguirre A., Schaye J., Hernquist L., Kay S., Springel V., Theuns T.: 2005, ApJ, 620L, 13A
- Aracil B., Petitjean P., Pichon C., Bergeron J.: 2004, A&A, 419, 811A
- Bahcall J.N.: 1966, ApJ, 146, 615B
- Bertone S., Stoehr F., White S.D.M.: 2005, MNRAS, 359, 1201B
- Bouché N., Murphy M.T., Péroux C., Csabai I. & Wild V.: 2006, MNRAS, 371, 495B
- Bruscoli M., Ferrara A., Marri S., Schneider R., Maselli A., Rollinde E. & Aracil B.: 2003, MNRAS, 343L, 41B
- Cen R., Miralda-Escud J., Ostriker J.P., Rauch M.: 1994, ApJ, 437L, 9C
- Cowie L.L., Songaila A., Kim T.-S., Hu E.M.: 1995, AJ, 109, 1522
- Cowie L. L., Songaila A.: 1998, Nat, 394, 44
- Davé R., Hernquist L., Weinberg D. & Katz N.: 1997, ApJ, 477, 21
- Davé R. and Oppenheimer B.D.: 2007, MNRAS, 374, 427D
- Dekel A. and Silk J.: 1986, ApJ, 303, 39D
- Desjacques V., Nusser A., Haehnelt M.G., Stoehr F.: 2004, MNRAS, 350, 879D
- Ellison S.L., Lewis G.F., Pettini M., Chaffee F.H., Irwin M.J.: 1999, Apj, 520, 456

Ferland G. J., Kosista K. T., Verner D. A., Ferguson J. W., Kingdom J. B. & Verner E. M.: 1998, *PASP*, 110, 761  
 Ferrara A. Scannapieco E. & Bergeron J.: 2005, *ApJ*, 634L, 37F  
 Ferrara A., Tolstoy E.:2000, *MNRAS*, 313, 291F  
 Haardt F. & Madau P.: 1996, *ApJ*, 461, 20  
 Haehnelt M.G., Steinmetz M., Rauch M.: 1996, *ApJ*, 465L, 95H  
 Heckman T.M., Lehnert M.D., Strickland D.K. & Armus L.: 2000, *ApJS*, 129, 493  
 Heger A., & Woosley S.E.: 2002, *ApJ*, 567, 532  
 Hopkins A. M.: 2004, *ApJ*, 615, 209H  
 Kawata, D., Rauch, M. 2007, submitted, astro-ph/0704652  
 Kim T.S., Carswell R.F., Cristiani S., D'odorico S., and Giallongo E.: 2002, *MNRAS*, 335, 555  
 Mac Low M. & Ferrara A.: 1999, *ApJ*, 513, 142M  
 Madau P., Ferrara A., Rees M.: 2001, *ApJ*, 555, 92M  
 Marri S. & White S.D.M.: 2003, *MNRAS*, 345, 561  
 Martin C.L.: 1999, *ApJ*, 513, 156  
 Martin C.L.: 2005, 621, 227  
 : Maselli A., Ferrara A., Bruscoli M., Marri S., Schneider R.: 2004, *MNRAS* 350L, 21M  
 Murray N., Quatert E. & Thompson T.A.: 2005, *ApJ*, 618, 569  
 Oppenheimer B.D. & Davé: 2006, *MNRAS*, 373, 1265O  
 Porciani C. & Madau P.: 2005, *ApJ*, 625, L43  
 : Ryan-Weber E.V., Pettini M., Madau P.: 2006, *MNRAS*, 371L, 78R  
 Scannapieco E., Ferrara A., & Madau P.: 2002, *Apj*, 574, 590  
 Scannapieco E.: 2005, *ApJ*, 624, L1  
 Schaye J., Rauch M., Sargent W.L.M., Kim T.S.: 2000, *ApJ*, 541, L1  
 Schaye J., Aguirre A., Kim T.-S., Theuns T., Rauch M. and Sargent W.L.W.: 2003, *ApJ*, 596, 768  
 Simcoe R.A., Sargent W.L.W., Rauch M.: 2004, *ApJ*, 606, 92S  
 Simcoe R.A.: 2006, *ApJ*, 653, 977S  
 Simcoe R.A., Sargent W.L.W., Rauch M. & Becker G.: 2006, *ApJ*, 637, 648S  
 Songaila, A.: 2001, *ApJ*, 561, L153  
 Songaila A.: 2005, *AJ*, 130, 1996  
 Springel V., Hernquist L.:2003, *MNRAS*, 339, 312S  
 Springel V., Yoshida N. & White S.D.M.: 2001 *ApJ*, 546, 665  
 Springel V.: 2005, *MNRAS*, 364, 1105  
 Telfer R.C., Kriss G.A., Zheng W., Davidsen A.F., Tytler D.: 2002, *ApJ*, 579, 500T  
 Theuns T., Leonard A., Efstathiou G., Pearce F.R. and Thomas P.A.: 1998, *MNRAS*, 301, 478  
 Verner D.A., Barthel P.D. and Tytler D.: 1994, *ApJ*, 108, 287  
 Woosley S.E., & Weaver T.A.: 1995, *ApJ*, 101, 181

## APPENDIX A: SYNTHETIC SPECTRA

### A1 Smoothing

To calculate a spectrum along a given line of sight (LOS) through the simulation box it is necessary to recover the physical properties of the gas at each point along the path,

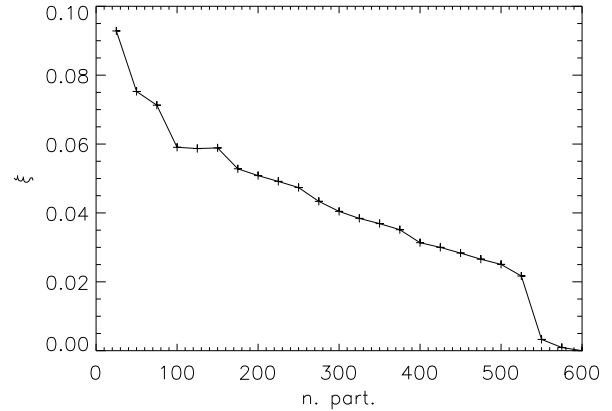


**Figure A1.** Smoothing convergence test using a gaussian kernel with a FWHM  $\sigma = 8.0 \text{ h}^{-1} \text{ kpc}$ .

by smoothing the various fields. For this, the line of sight has been divided into cells, to which the values of the gas density, temperature, velocity, and metallicity are assigned by a weighted mean on the surrounding particles. The weight of each particle is determined by its distance from the LOS-cell using a specified kernel function. For consistency with the adopted SPH simulation, we have chosen a gaussian kernel with FWHM  $\sigma = 8.0 \text{ h}^{-1} \text{ kpc}$  comoving. The number of particles used to derive the mean is fixed by the balance between convergence and computational expense. To determine such number, we have recovered the various physical quantities for 600 cells along the LOS using a variable number of particles (up to 600, the reference case). In Fig. A1 we plot the results of such test in terms of the quantity

$$\xi_j = \left\langle \frac{|X_i^j - X_{600}^j|}{X_{600}^j} \right\rangle_j \quad (\text{A1})$$

where  $X_i^j$  indicates the  $j$ -th physical quantity recovered using  $i$  particles, and the mean is calculated over the cells considered. As we see, an accuracy of  $\lesssim 6\%$  is obtained by using 100 particles; by further taking into account the computational expense, we have fixed this value as the optimal one and have adopted it in the following.

To further test the smoothing algorithm, we have recovered the physical properties of 1000 gas particles. Fig. A2 shows a comparison between recovered and simulated values. The accuracy of recovered quantities is reasonably good. The scatter in the distribution may be related to particles belonging to regions near the interfaces of virializing halos, the sharp transition across the shock front characterizing these regions been smoothed away by the recovery process. This interpretation is supported by the ‘‘wall’’ in the temperature distribution at  $T \simeq 10^4 \text{ K}$ , i.e. the lowest temperature allowed by the adopted atomic cooling function. Moreover, the small filling factor of virialized regions tends to translate into a density overestimate. The velocity distribution seems instead more symmetric, as a result of the different kinetic behavior characterizing the collapsed haloes distribution. The metallicity field is particularly affected by the recovery process, as expected from the fact that no diffusion equations are solved for the heavy elements. As a result, polluted and pristine regions are separated by unphysical sharp

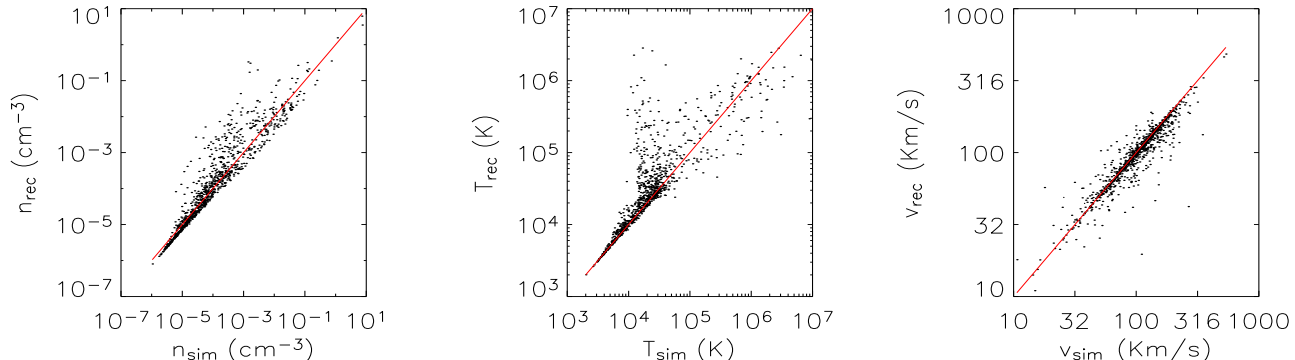


**Figure A2.** Smoothing recovery test for the density (left panel), temperature (middle) and velocity (right) fields. The dots represent the relation between the recovered and the simulated physical properties of 1000 particles in the high resolution simulation at redshift  $z \sim 3.0$ . The line represents the case of an ideal recovery algorithm.

| $z$   | QSO           |
|-------|---------------|
| 2.170 | Q0122 – 380   |
| 2.208 | PKS1448 – 232 |
| 2.280 | HE0001 – 2340 |
| 2.406 | Q0109 – 3518  |
| 2.406 | HE2217 – 2818 |
| 2.434 | HE1347 – 2457 |
| 2.740 | HE0151 – 4326 |
| 2.758 | Q0002 – 422   |

**Table A1.** QSOs spectra used to compute the models for  $S/N$  and  $S/E$  ratios for the UVES spectrograph.

| $z$   | QSO           |
|-------|---------------|
| 2.134 | HE1341 – 1020 |
| 2.685 | PKS0329 – 255 |
| 2.661 | Q0453 – 423   |
| 2.885 | HE2347 – 4342 |
| 3.054 | HE0940 – 1050 |

**Table A2.** QSOs spectra used to test the models for  $S/N$  and  $S/E$  ratios for the UVES spectrograph.

boundaries. Results concerning the metallicity derived from our synthetic spectra should be taken with caution.

## A2 UVES models

For our synthetic spectra we have chosen to mimic the behavior of the UVES spectrograph mounted at the ESO Very Large Telescope (VLT). To obtain a reliable model for the signal to noise ( $S/N$ ) and for the signal to error ( $S/E$ ) ratio we have used a set of observations made as part of the Large Program “*The cosmic evolution of the IGM*” (J. Bergeron *et al.*) which provides high  $S/N$ , high spectral resolution IGM data for  $z \simeq 3$  (Tab. A1).

Considering that the maximum restframe absorption wavelength used in our spectra is  $\lambda \simeq 1550 \text{ \AA}$ , we have fixed the wavelength range for our models to  $3300 < \lambda < 7400 \text{ \AA}$ .

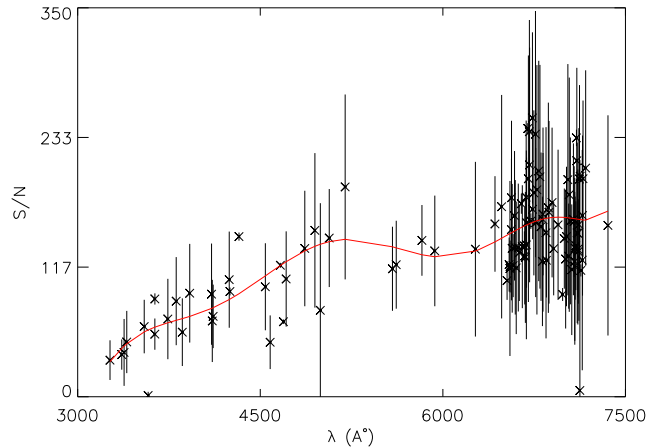


**Figure A3.** Fiducial model of the  $S/N$  for the UVES spectrograph. In black we show the observed data, along with their variance; while the red line refers to our polynomial fit. We can note the different density of data with  $\lambda$ , this reflects the varying number density of the absorbing clouds.

### A2.1 $S/N$ model

To obtain the  $S/N$  dependence with wavelength we have searched (by eye) for unabsorbed regions in the UVES spectra listed in Tab. A1. The data obtained then were binned in  $0.25 \text{ \AA}$  bins, so that every bin is formed by 10 pixels at the UVES resolution of  $\simeq 0.025 \text{ \AA}$  per pixel. We then have considered the mean value as estimate for the signal from each pixel/bin, the noise was estimated by a simple subtraction. The triplet of values ( $\lambda$ - $S$ - $N$ ) obtained in this way were collected in a single large sample sorted by wavelengths. To reduce the data used for the fitting, we have divided the final data set in bins of 100 values. For each bin we then have estimated the mean value and the scatter for the  $S/N$  by fitting the distribution of values using a gaussian. The values obtained were then fitted using a polynomial function (Fig. A3). In Fig. A4 we show the test of our fiducial model for the  $S/N$  using the QSOs given in Tab. A2. We have plotted the distribution of the absolute scatter between predicted

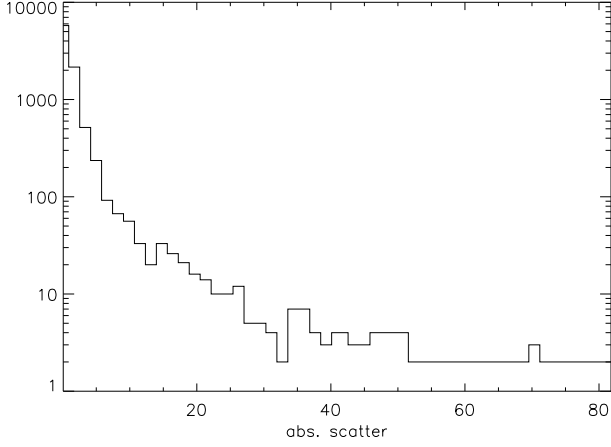


**Figure A4.** Test for the  $S/N$  model (Fig. A3). The steep decrease in the scatter distribution indicates a satisfactory model behavior.

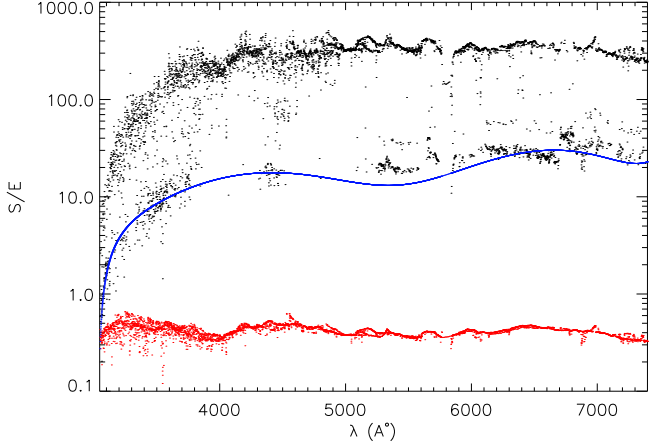


**Figure A6.** Test for our  $S/E$  model. The colors are as in Fig. A5.

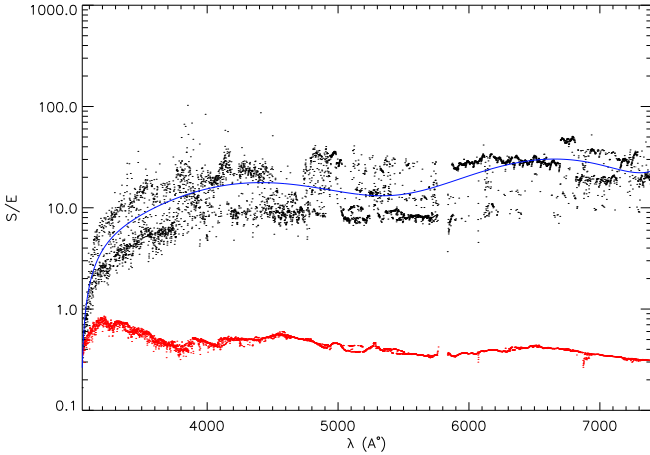


**Figure A5.** Dependence of the  $S/E$  with wavelength. The black dots refer to the observed data, while the blue line represents our polynomial fit. Red dots represent the predicted ratios using the Poissonian approximation.

and observed  $S/N^4$ . As we can see, also if the distribution reaches high values; the rapid decrease of the observed histogram satisfies our model.

### A2.2 $S/E$ model

To obtain a model for the signal-to-error ratio, we have treated the observed data as described in the previous section. In Fig. A5 we show the observed data (black dots) along with our model (blue dots) and a Poissonian model (red dots). We see how the latter approximation (usually considered) overestimates the errors associated with fluxes. From Fig. A6 we can see that both the approximations overestimate the errors associated with fluxes. However, our model can be considered as a better low-limit approximation to the real ratio.

<sup>4</sup> The data were treated in the same way as for the model.

### A2.3 Binning issues

To assess the dependencies of our  $S/N$  model, we have carried out the binning procedure using different bin sizes. In Fig. A7 we show on the left our results for binning sizes of 0.25, 0.50, 0.75, 1.0, 2.0, 4.0 Å, respectively, as dots with colors from black to red. The right plot shows the mean relative scatter of each data set, from the reference one (that relative to a 0.25 Å binning).

These two plots demonstrate that the main consequence of rebinning is a lowering of the observed  $S/N$  ratio, most probably due to the intrinsic continuum variation inside the bin. Since we do not have fully analyzed spectra, and considering that every new set of  $S/N$  data lies into the error bars of our reference-data set, we can consider our model as acceptable.

### A3 Spectrum generation and degradation

To obtain the absorption arising along the LOS, that means the optical depth  $\tau$  for each cell, we have used the Eq. A2 (Theuns et al. 1998):

$$\tau(k) = \sum_{i=1}^{N_{px}} n_x(i) \Delta_{px} \frac{(\sigma_0 f \lambda_0)}{1+z} \frac{c}{\sqrt{\pi} b_x(i)} \Phi_{V_{oigt}}(k, i) \quad (\text{A2})$$

$$n_x(i) = (Z_{II}(i) Y_{II,x}(i) + Z_{III}(i) Y_{III,x}(i)) n(i) f(A_x, \chi_+) \quad (\text{A3})$$

where:

- (i)  $k$  is the cell where we want to calculate the optical depth;
- (ii) the summation is over all the cells,  $N_{px}$ , in each LOS;
- (iii)  $n_x(i)$  is the numeric density in the cell  $i$  of the element  $x$  with ionization degree  $\chi_+$ ;
- (iv)  $n(i)$  is the total gas density in the cell  $i$ ;
- (v)  $Y_{II,x}$  and  $Y_{III,x}$  are the yields for the element  $x$ , respectively for PopII and PopIII stars (Tab. A3);
- (vi)  $f(A_x, \chi_+)$  is the ionization fraction;
- (vii)  $\Delta_{px}$  is the linear dimension of the cell;
- (viii)  $z$  is the redshift;
- (ix)  $\sigma_0$ ,  $f$ ,  $\lambda_0$  are atomic constants, respectively:  $\sigma_0$  is linked to the Thomson cross section,  $\sigma_T$ , as follow  $\sigma_0 =$



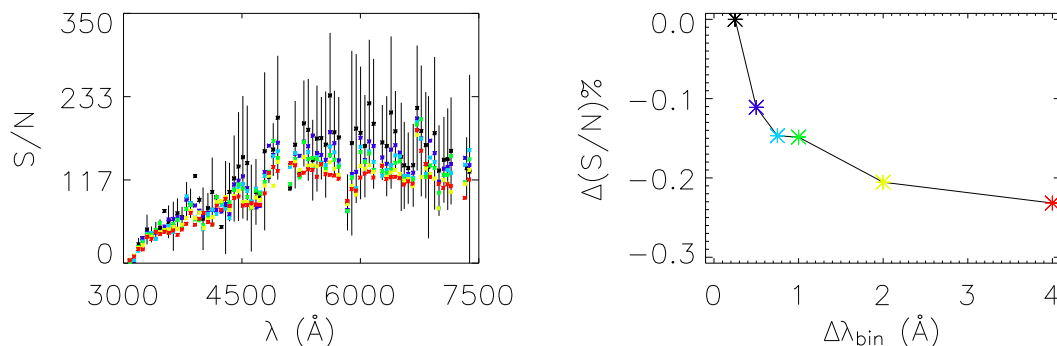


**Figure A7.** Dependencies of the  $S/N$  model on the binning size. On the left we show the observed  $S/N$  ratio for different wavelengths. Colors, from black to red, refer to a growing binning size (0.25, 0.50, 0.75, 1.0, 2.0, 4.0 Å). For the first binning size (our working size) we show also the relative errors. The right plot shows the observed mean relative scatter of each set from the reference one as a function of the binning size.

| Element | PopIII | PopII  |
|---------|--------|--------|
| C       | 0.0488 | 0.109  |
| Ø       | 0.504  | 0.693  |
| Si      | 0.211  | 0.0626 |

**Table A3.** Yields for the element included in our spectra (Woosley & Weaver (1995), Heger & Woosley (2002)).

$\sqrt{\frac{3\pi}{8}\sigma_T}$ , and  $f$  is the oscillator strength for the transition  $\lambda_0^5$ ;

(x)  $b_x$  is the Doppler parameter for the element  $x$  defined as:

$$b_x(i) = \sqrt{\frac{2kT(i)}{m_x}} \simeq 12.845 \sqrt{\frac{T_4(i)}{A_x}} \text{ km s}^{-1} \quad (\text{A4})$$

where:  $k$  is the Boltzmann constant,  $T(i)$  is the temperature of the  $i$ -th cell in Kelvin<sup>6</sup>,  $m_x$  and  $A_x$  are respectively the mass and the atomic number of the element  $x$ ;

(xi)  $\Phi_{Voigt}(k, i)$  is the statistical weight that determine the contribution of the cell  $i$ -th to the absorption of the cell  $k$ -th, in our case we have chosen to use a Voigt profile.

The absorption wavelength associated to each  $\tau(k)$  is obtained considering the rest-frame absorption wavelength at the redshift of the numerical output<sup>7</sup> and the total velocity of the cell. To compare with the data, it is necessary to degrade the raw spectrum to account for finite instrumental resolution and noise. To this aim we convolve the spectra with the (UVES) instrumental profile assumed to be a gaussian of width  $\simeq 6.6 \text{ km s}^{-1}$ . The noise contribution to the flux in each bin is obtained by considering a gaussian noise with zero mean and with width determined by our  $S/N$  model. The same is done for the error associated with each flux value. In Tables A4 and A5 we list the atomic parameters for the atomic transition included in our simulated

spectra. Here we show respectively in the first column the designation for the absorption followed by the rest frame absorption wavelength, oscillator strength, gamma value and the second absorption wavelength in case of a doublet.

## APPENDIX B: SAMPLE SPECTRA

In the following Figs. B1 - B10 we show the simulated spectra along a slice of the simulated volume containing the target galaxy.

<sup>5</sup> The atomic parameters for each transition were taken from Verner et al. (1994).

<sup>6</sup>  $T_4 \equiv T/10^4 \text{ K}$ .

<sup>7</sup> The redshift difference between two cells is less than 0.01%.

| Ion       | $\lambda_1(\text{\AA})$ | f      | $\gamma/10^9$ | $\lambda_2(\text{\AA})$ |
|-----------|-------------------------|--------|---------------|-------------------------|
| CIV1548   | 1548.195                | 0.190  | 0.2650        | 1550.770                |
| OII1302   | 1302.168                | 0.0504 | 0.5750        | —                       |
| OVI1031   | 1031.926                | 0.133  | 0.4.125       | 1037.617                |
| SiII1526  | 1526.707                | 0.132  | 1.9600        | —                       |
| SiII1304  | 1304.370                | 0.0871 | 1.7200        | —                       |
| SiII1260  | 1260.422                | 1.180  | 2.5330        | —                       |
| SiII1193  | 1193.290                | 0.584  | 3.4950        | —                       |
| SiII1190  | 1190.416                | 0.293  | 3.5030        | —                       |
| SiIII1206 | 1206.500                | 0.0168 | 2.550         | —                       |
| SiIV1393  | 1393.755                | 0.524  | 0.88250       | 1402.770                |

**Table A4.** Atomic parameters for the metals transitions included in our simulated spectra (Verner et al. 1994).  $\lambda_2$  refers to the second component in doublets.

| Ion    | $\lambda_1(\text{\AA})$ | f                     | $\gamma/10^7$ |
|--------|-------------------------|-----------------------|---------------|
| HI1216 | 1215.670                | 0.416                 | 62.650        |
| HI1026 | 1025.722                | 0.0791                | 18.970        |
| HI972  | 972.537                 | 0.0290                | 8.126         |
| HI950  | 949.743                 | 0.0139                | 7.640         |
| HI938  | 937.804                 | $0.780 \cdot 10^{-2}$ | 4.4230        |
| HI931  | 930.748                 | $0.481 \cdot 10^{-2}$ | 1.236         |
| HI926  | 926.226                 | $0.318 \cdot 10^{-2}$ | 0.8249        |
| HI923  | 923.150                 | $0.222 \cdot 10^{-2}$ | 0.5782        |
| HI921  | 920.963                 | $0.160 \cdot 10^{-2}$ | 0.4208        |
| HI919  | 919.351                 | $0.120 \cdot 10^{-2}$ | 0.3158        |
| HI918  | 918.129                 | $0.921 \cdot 10^{-3}$ | 0.2430        |
| HI917  | 917.181                 | $0.723 \cdot 10^{-3}$ | 0.1910        |
| HI916  | 916.429                 | $0.577 \cdot 10^{-3}$ | 0.1529        |

**Table A5.** Atomic parameters for the HI included in our simulated spectra (Verner et al. 1994).

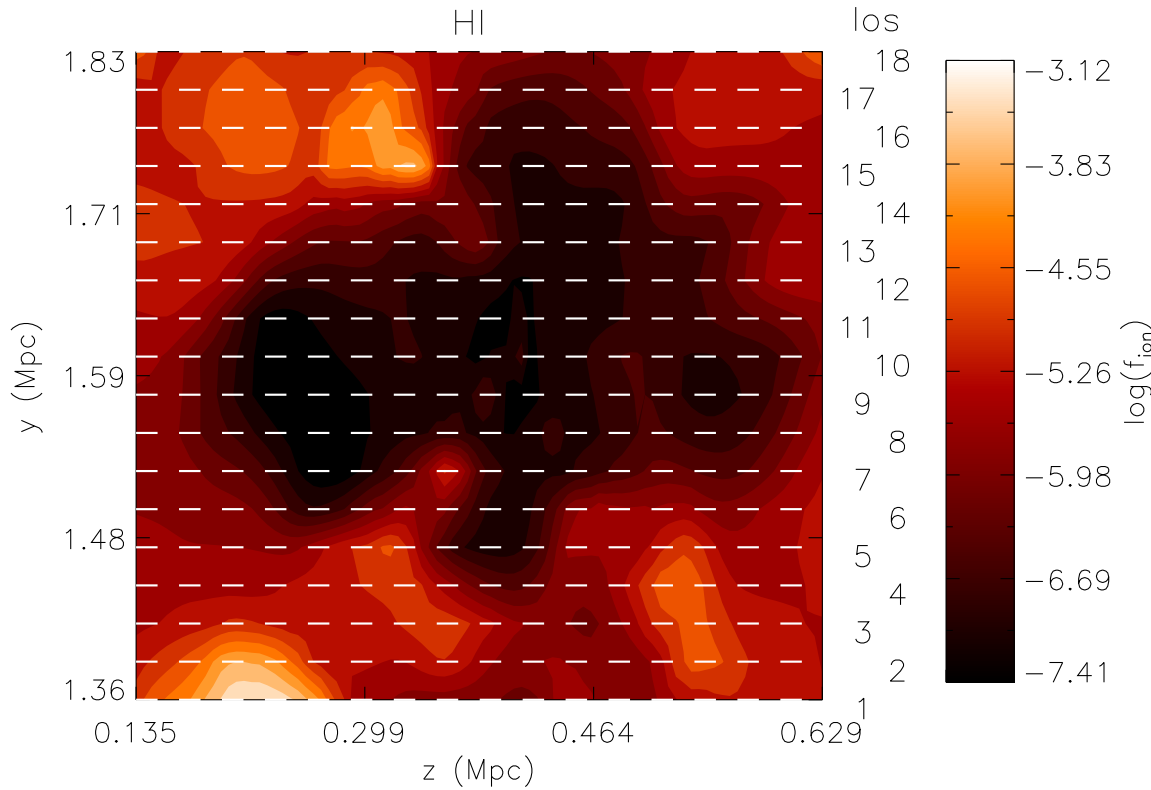
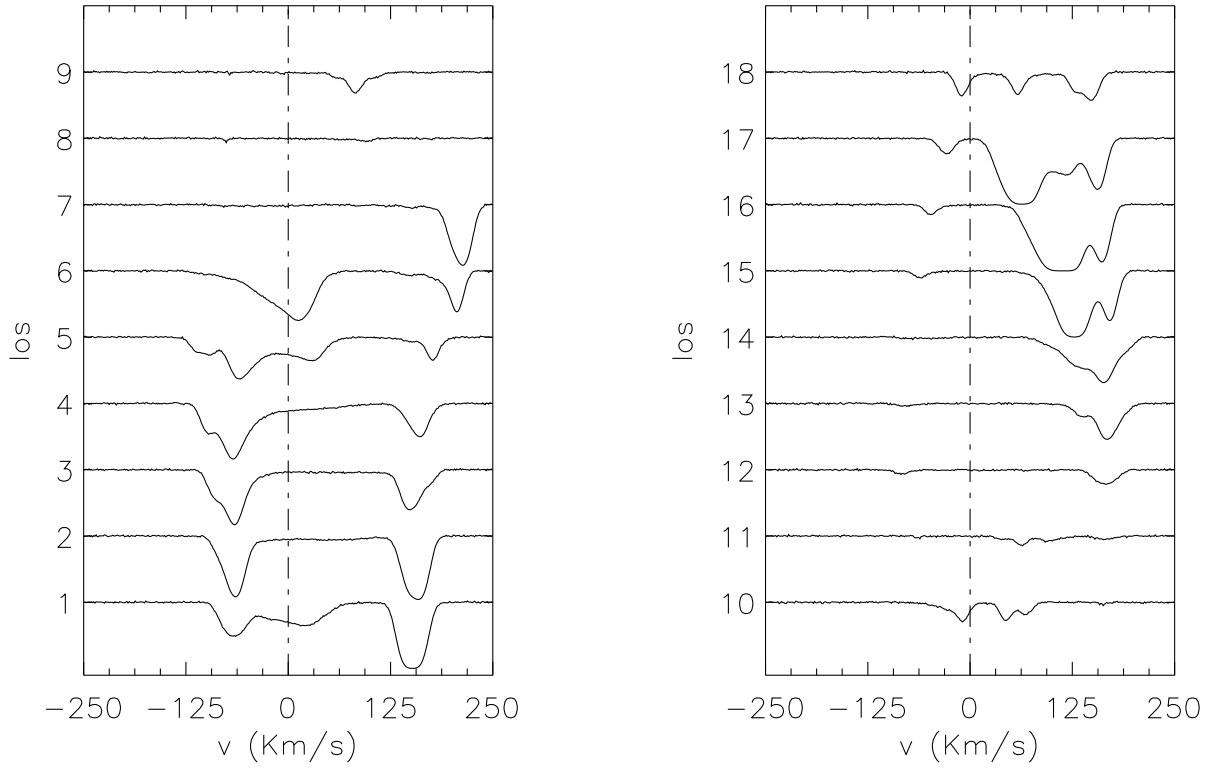


**Figure B1.** The map shows for the ionization fraction of the ion indicated by the label. The dotted lines identify by progressive number the LOS whose spectra are shown in the upper panels, For ions not discussed in detail, we show in the upper panel the expected column density derived from an integration along each LOS.

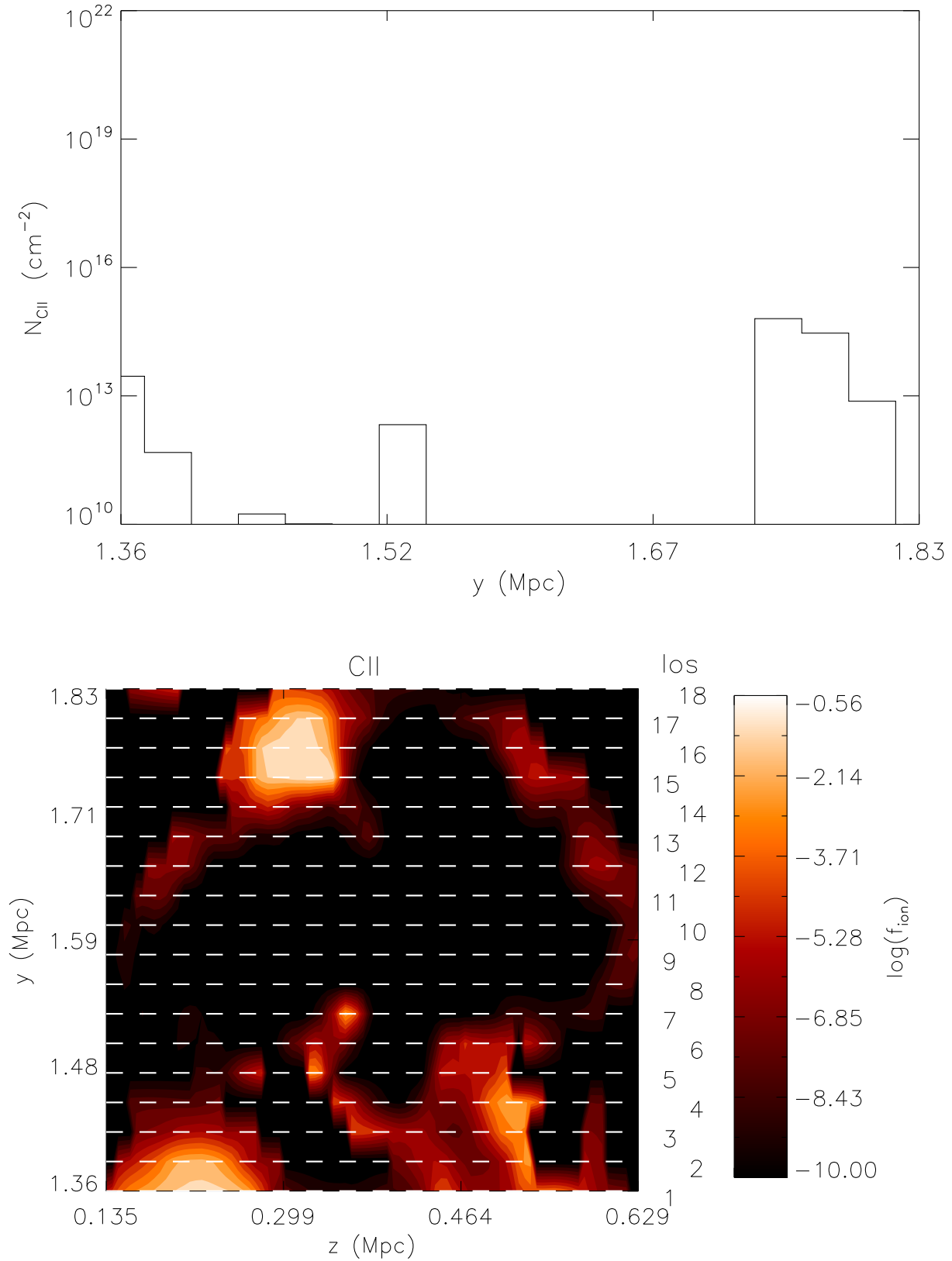


**Figure B2.**

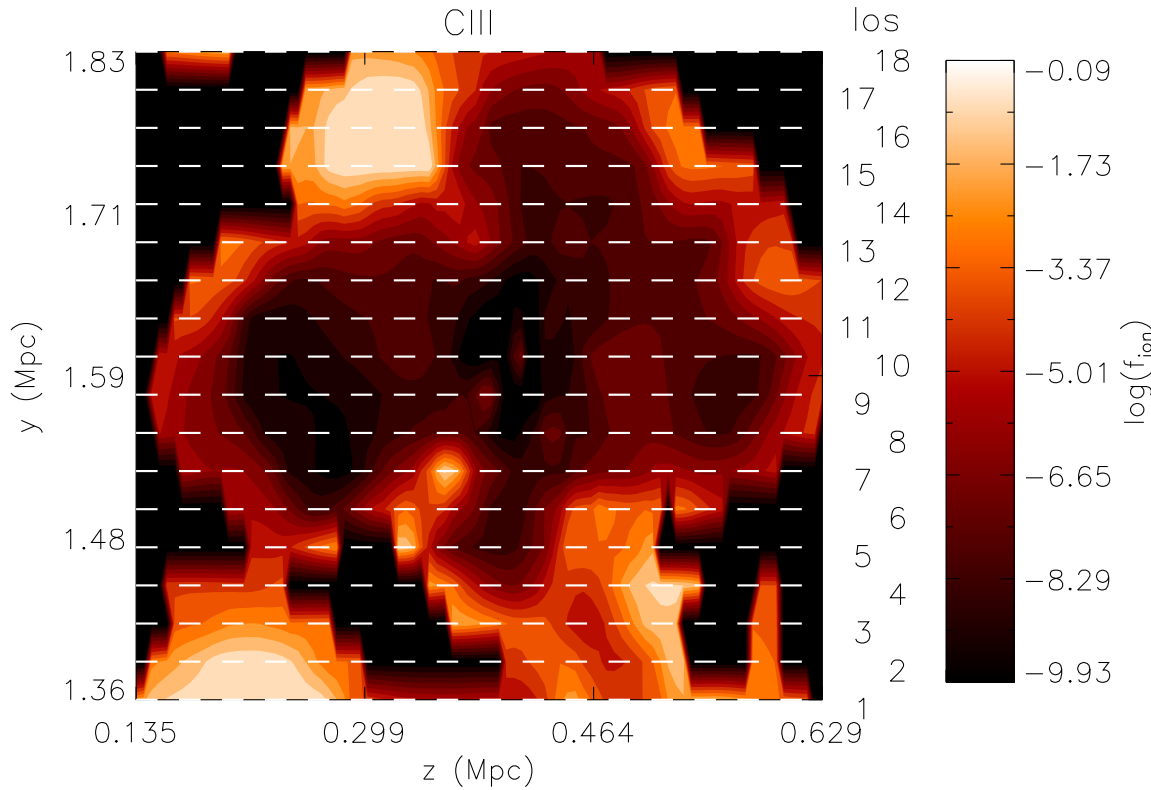
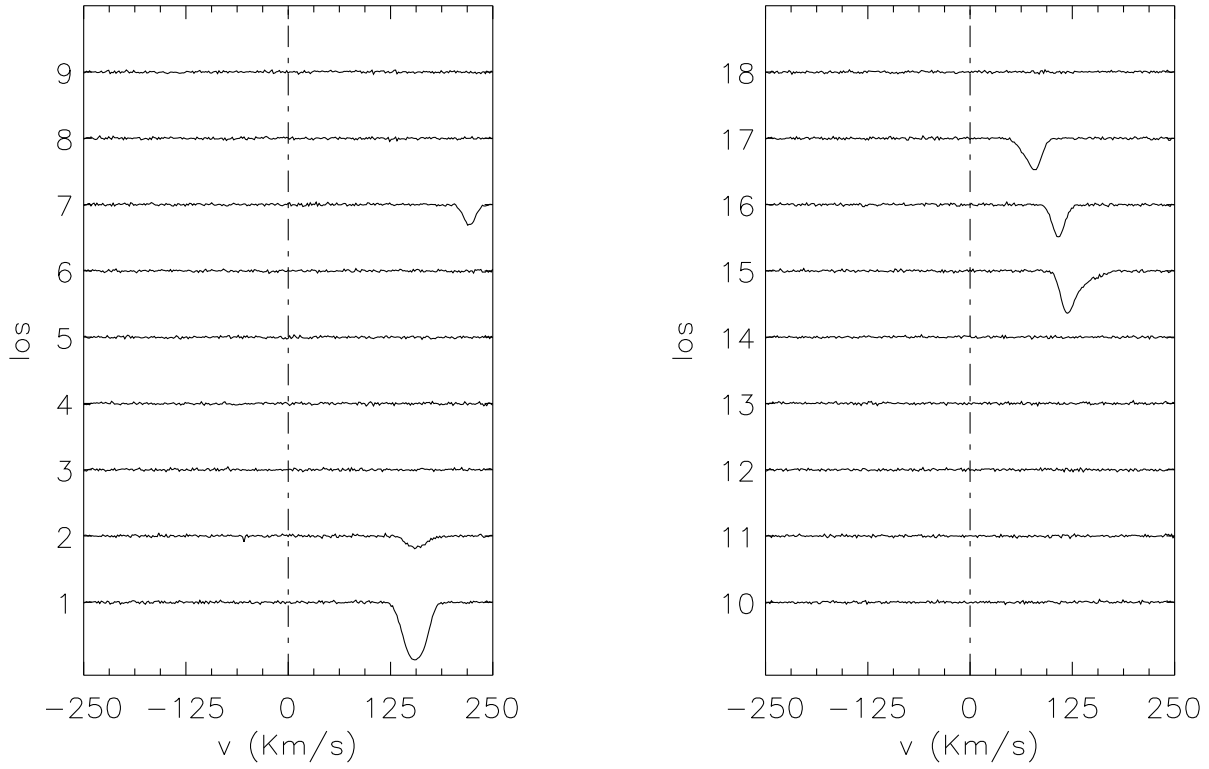
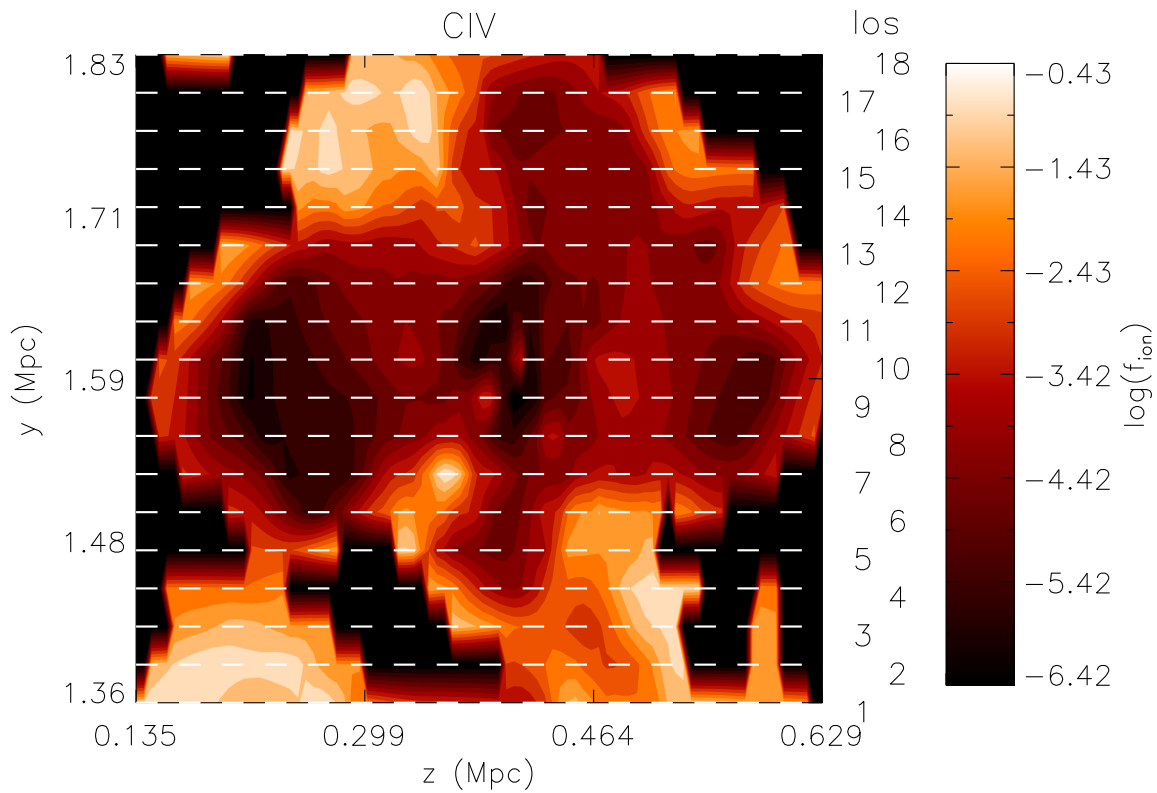
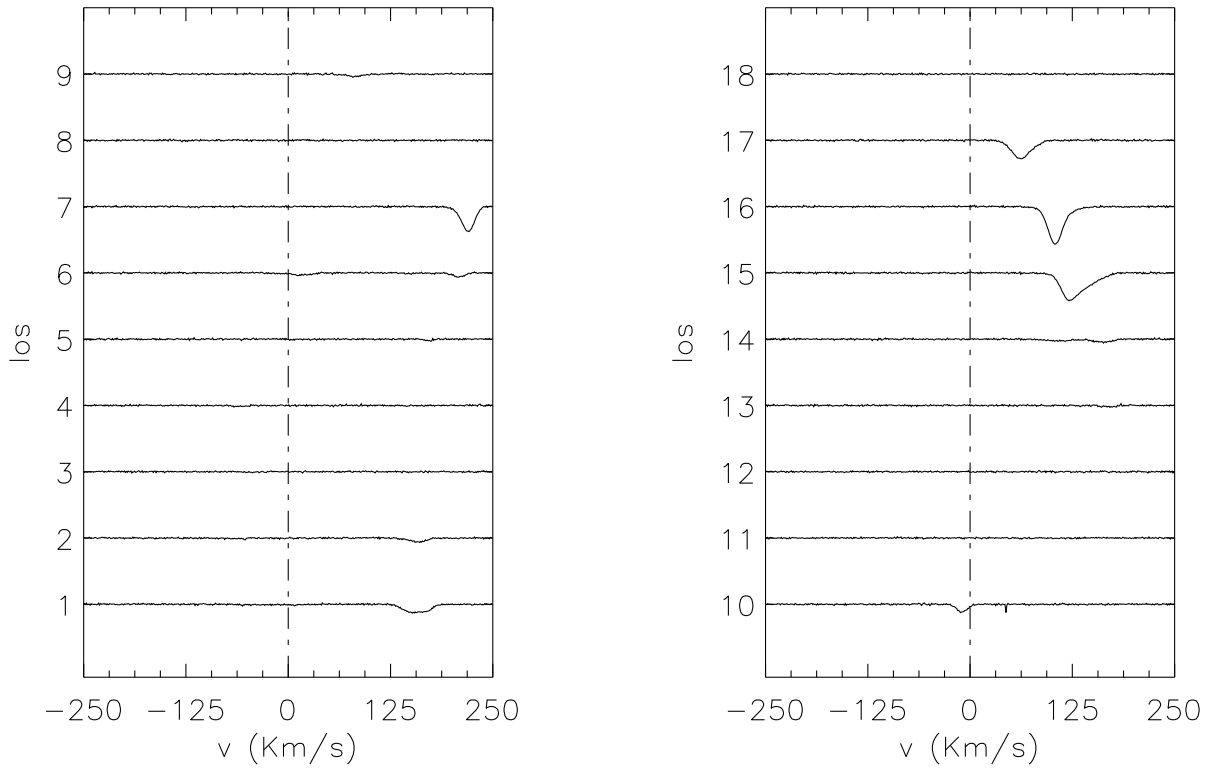


Figure B3.



**Figure B4.**

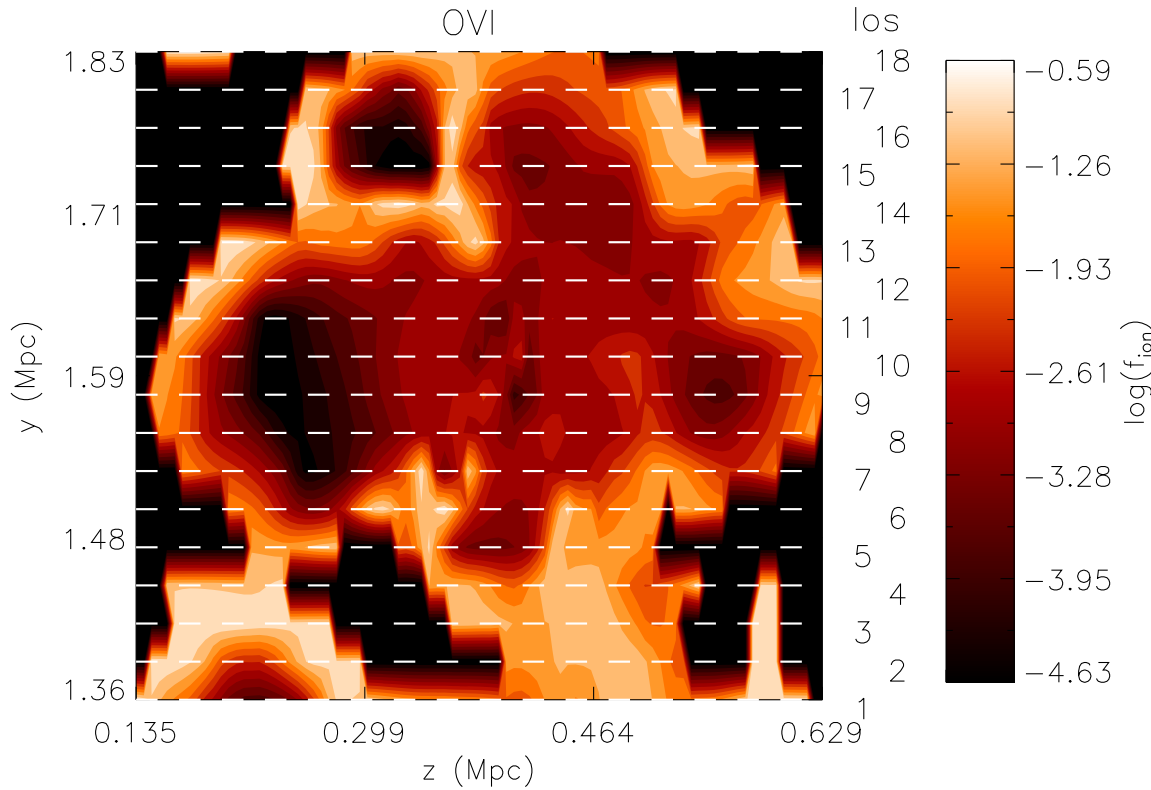
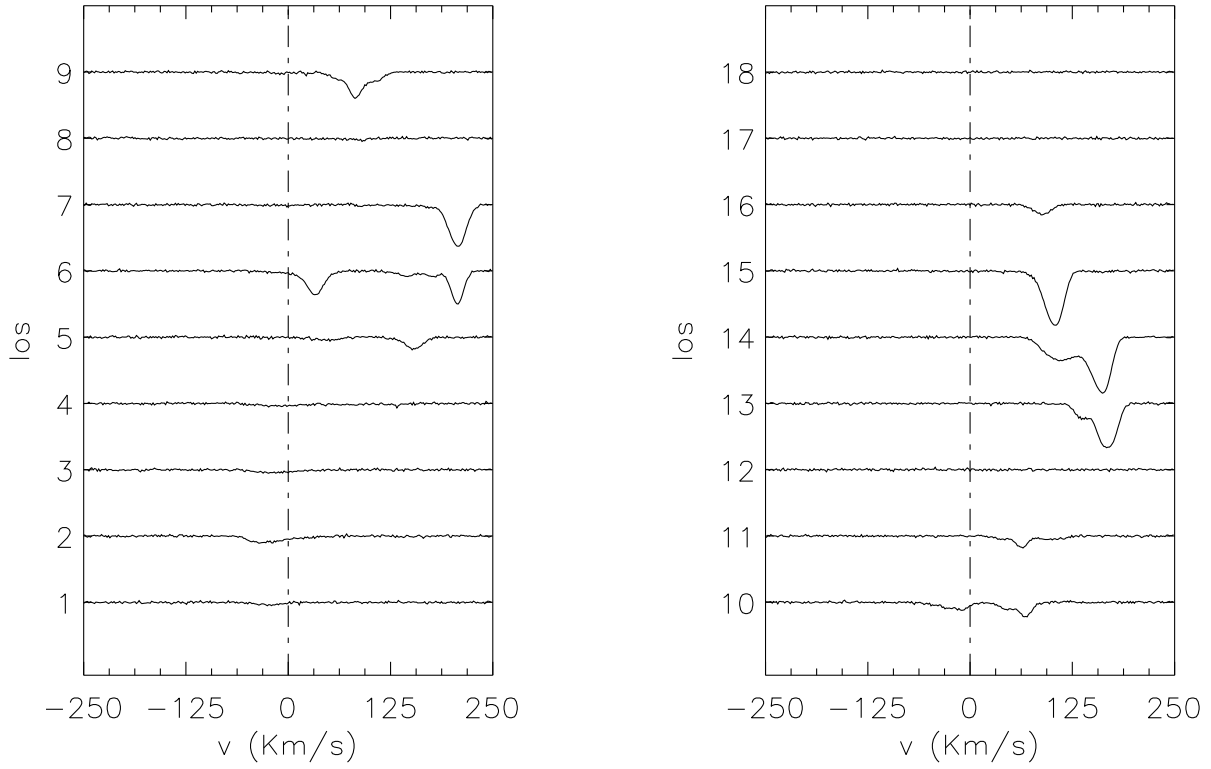
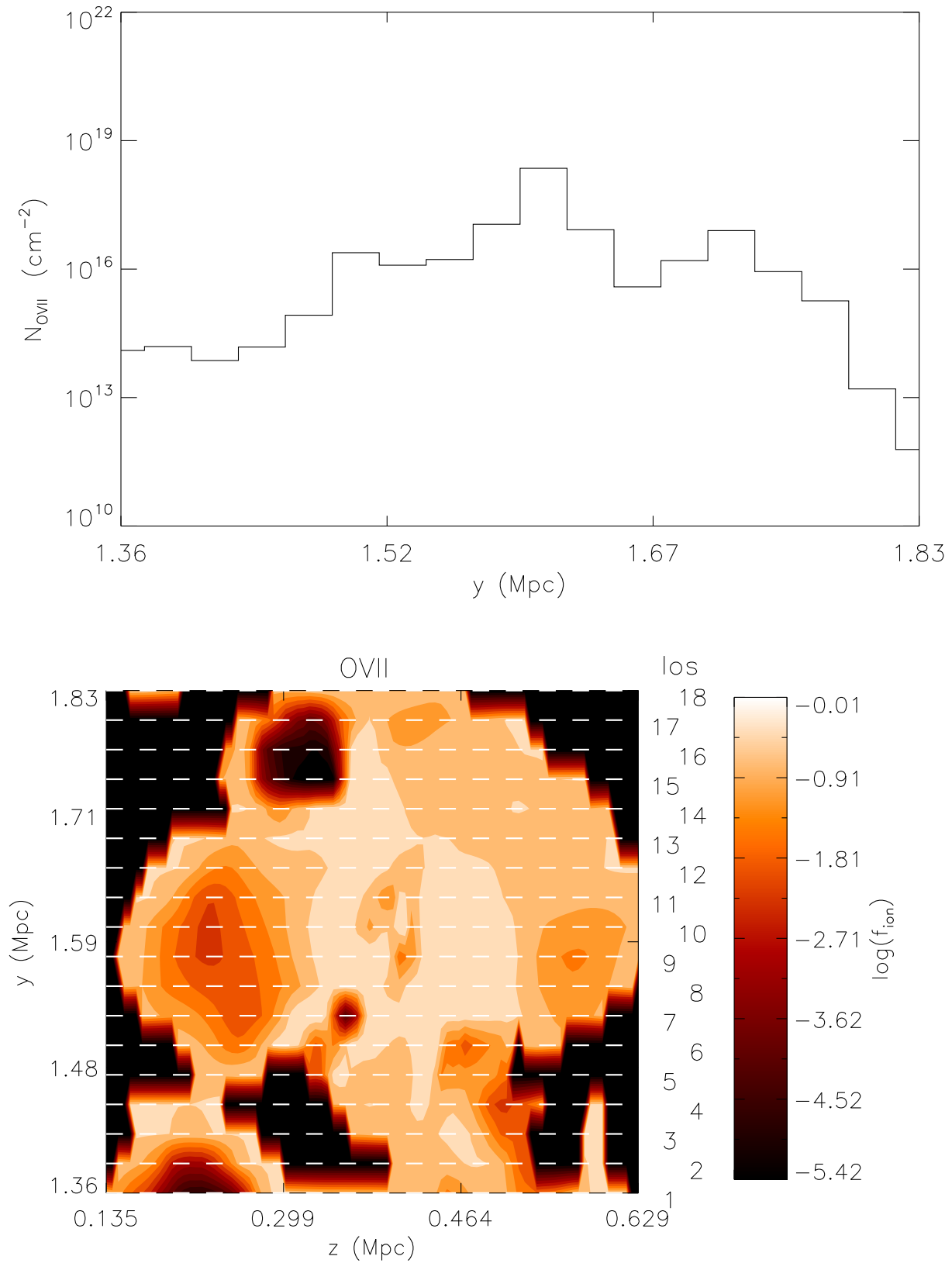


Figure B5.



**Figure B6.**



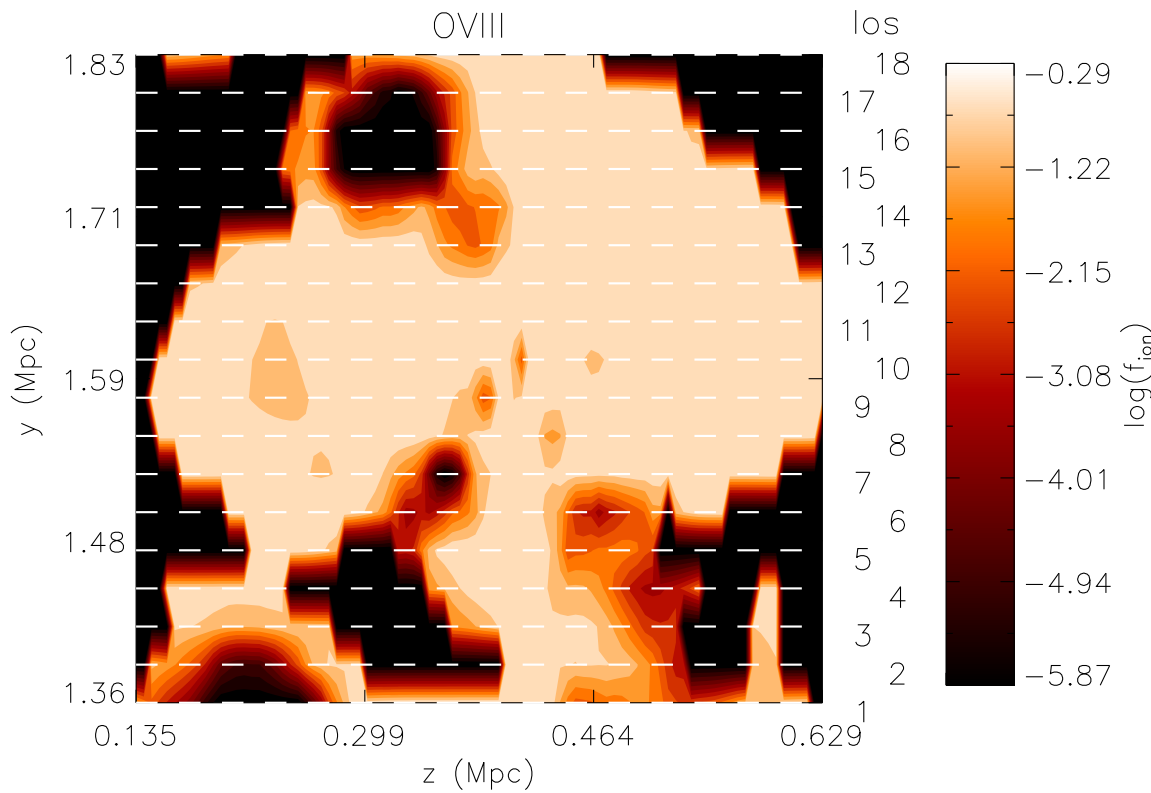
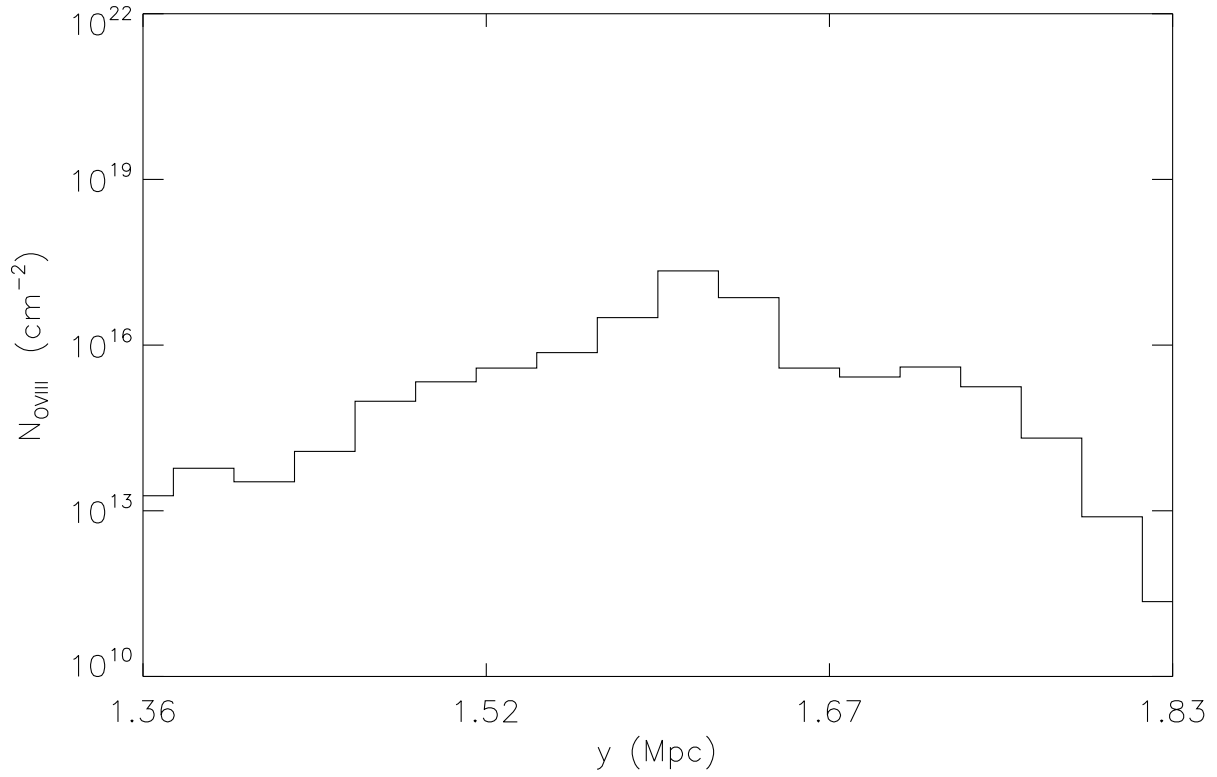
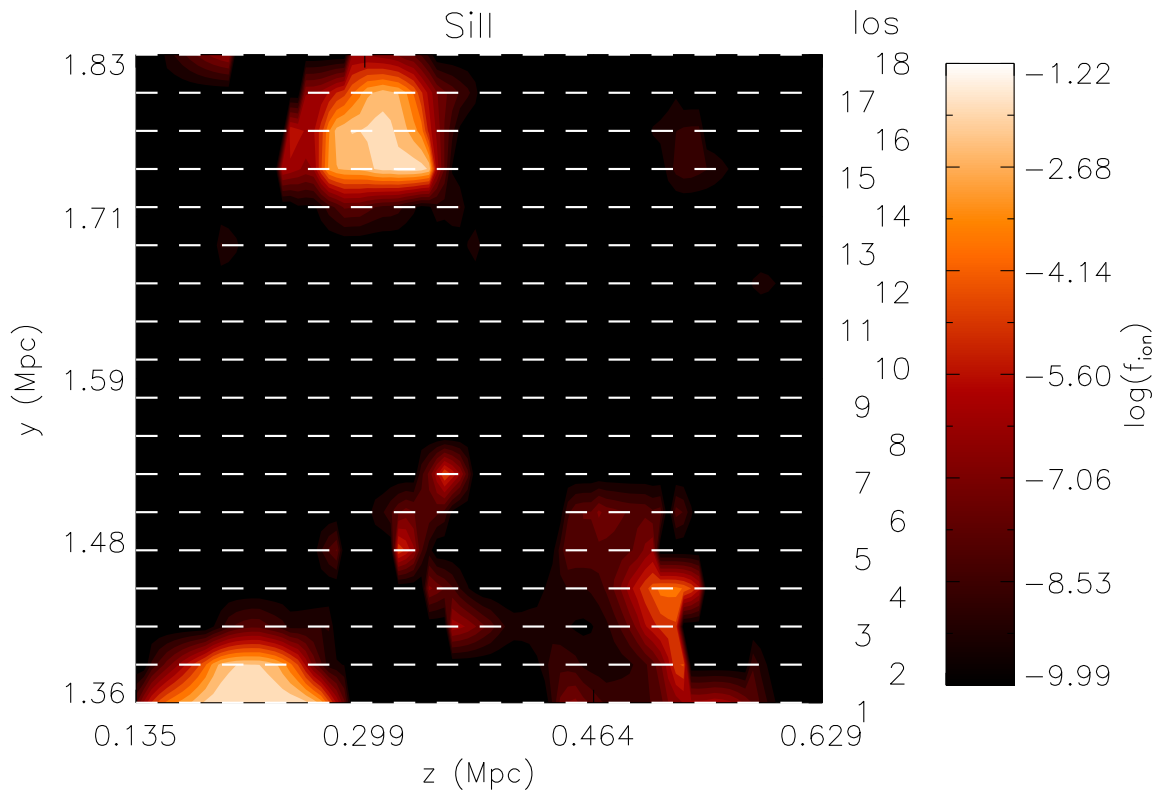
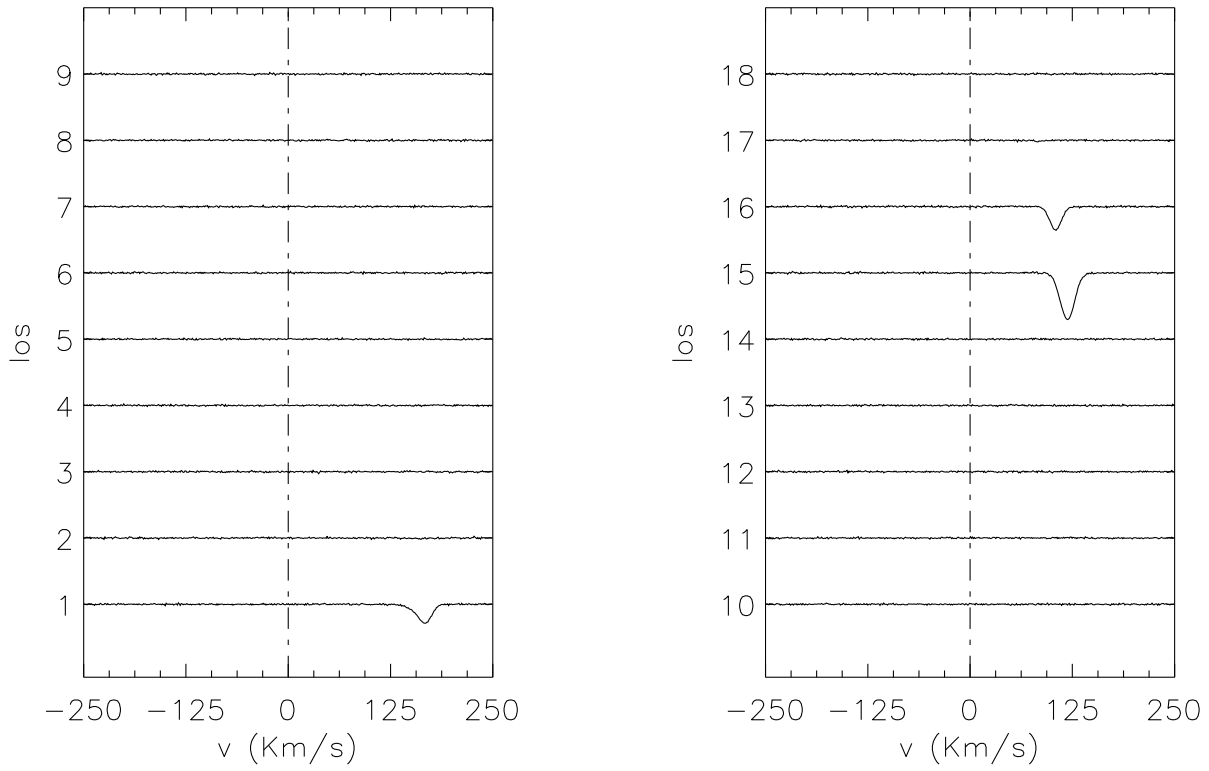


Figure B7.



**Figure B8.**

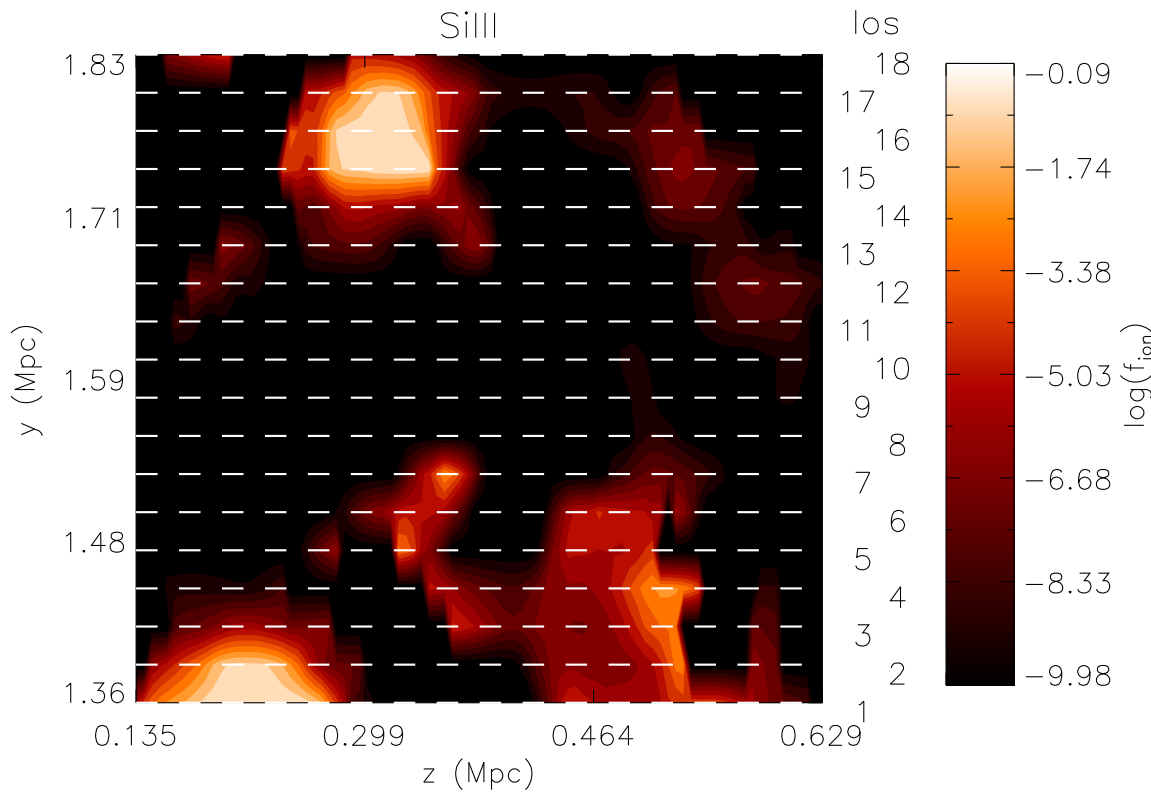
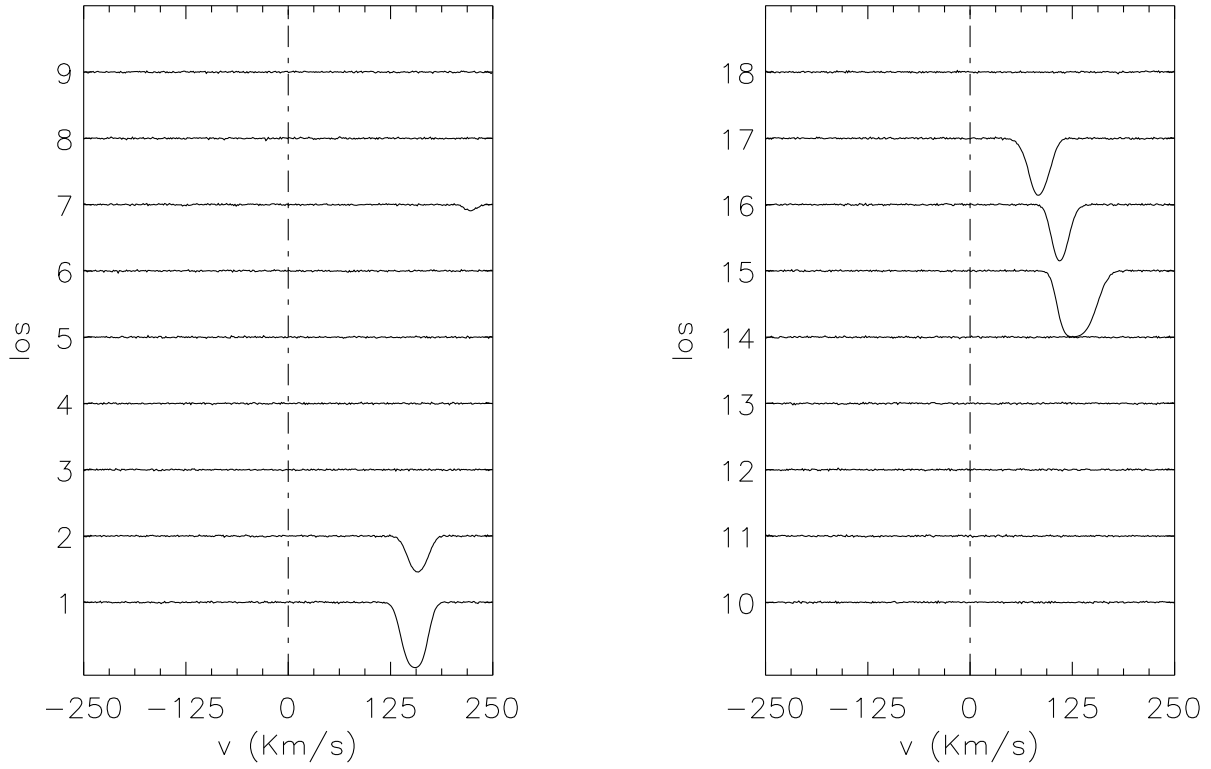
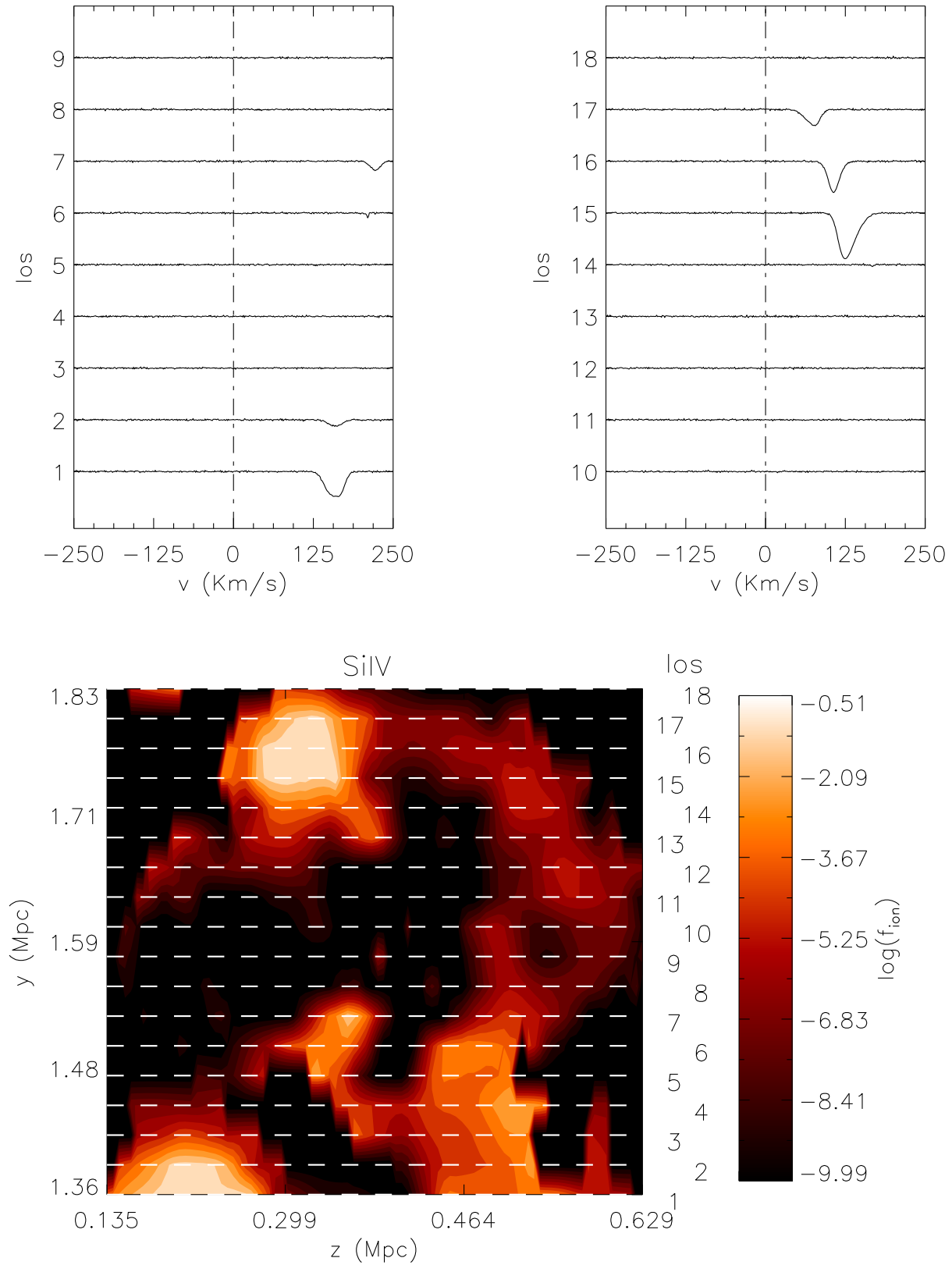


Figure B9.



**Figure B10.**